Hard hexagon partition function for complex fugacity

M. Assis[1], J.L. Jacobsen[2,3], I. Jensen[4], J-M. Maillard[5] and B.M. McCoy[1]

[1] CN Yang Institute for Theoretical Physics, State University of New York, Stony Brook, NY, 11794, USA

[2] Laboratoire de Physique Théorique, École Normale Supérieure, 24 rue Lhomond, 75231 Paris Cedex, France

3 Université Pierre et Marie Curie, 4 Place Jussieu, 75252 Paris, France

[4] ARC Center of Excellence for Mathematics and Statistics of Complex Systems, Department of Mathematics and Statistics, The University of Melbourne, VIC 3010, Australia

[5] LPTMC, UMR 7600 CNRS, Université de Paris, Tour 23, 5ème étage, case 121, 4 Place Jussieu, 75252 Paris Cedex 05, France

Abstract.

We study the analyticity of the partition function of the hard hexagon model in the complex fugacity plane by computing zeros and transfer matrix eigenvalues for large finite size systems. We find that the partition function per site computed by Baxter in the thermodynamic limit for positive real values of the fugacity is not sufficient to describe the analyticity in the full complex fugacity plane. We also obtain a new algebraic equation for the low density partition function per site.

1. Introduction

The hard hexagon model was solved by Baxter over 30 years ago [1, 2]. More precisely Baxter computed the thermodynamic limit of the grand partition function per site for real positive values of the fugacity z

$$\lim_{L_v, L_h \to \infty} Z_{L_v, L_h}^{1/L_v L_h}(z) \qquad \text{with} \qquad 0 < L_v/L_h < \infty \qquad \text{fixed.} \tag{1}$$

Even more precisely Baxter computed the limit

$$\kappa(z) = \lim_{L_h \to \infty} \lambda_{\max}(z; L_h)^{1/L_h}, \tag{2}$$

where $\lambda_{\max}(z; L_h)$ is the largest eigenvalue of the transfer matrix. Baxter found that there are two distinct regions of positive fugacity

$$0 \leq z < z_c \qquad \text{and} \qquad z_c < z < \infty, \tag{3}$$

with

$$z_c = \frac{11 + 5\sqrt{5}}{2} = 11.0901699473 \cdots, \tag{4}$$

where in each separate region the partition function per site has separate analytic expressions, which we denote by $\kappa_-(z)$ for the low density, and by $\kappa_+(z)$ for the high density intervals respectively. The low density function $\kappa_-(z)$ has branch points at z_c and

$$z_d = -\frac{1}{z_c} = \frac{11 - 5\sqrt{5}}{2} = -0.0901699473 \cdots, \tag{5}$$

is real and positive in the interval $z_d \leq z \leq z_c$ and is analytic in the plane cut along the real axis from z_d to $-\infty$ and z_c to $+\infty$. Conversely the high density function $\kappa_+(z)$ is real and positive for $z_c \leq z < +\infty$ and is analytic in the plane cut along the real axis from z_c to $-\infty$.

For the purpose of thermodynamics it is sufficient to restrict attention to positive values of the fugacity. However, it is of considerable interest to investigate the behavior of the partition function for complex values of z as well. For finite size systems the partition function is, of course, a polynomial and as such can be specified by its zeros.

In the thermodynamic limit the free energy will be analytic in all regions which are the limit of the zero free regions of the finite system [3]. In general there will be several such regions. One such example with three regions is given by Baxter [4]. There appears to be no general theorem stating when the free energy of a system can be continued through the locus of zeros.

The analytic structure of the free energy in the complex fugacity plane is not in general determined by the the free energy on the positive z axis and for hard hexagons it is only for the positive z axis that a complete analysis has been carried out. In this paper we address the problem of determining analyticity in the complex z plane by computing the partition function zeros on lattices as large as 39×39 and comparing these zeros with the locus computed from the limiting partition functions per site computed by Baxter for real positive value for the fugacity $0 \leq z \leq \infty$. We will see that the two functions $\kappa_\pm(z)$ are not sufficient to describe the location of the zeros in the complex z plane. There is, of course, no reason that $\kappa_\pm(z)$ should be sufficient to represent the partition function in the entire complex z plane. We propose in section 6.2 an extension of Baxter's methods which can explain our results in the portion of the complex plane not covered by $\kappa_\pm(z)$.

In section 2 we present the relation between partition function zeros and the eigenvalues of the transfer matrix with special attention to the differences between cylindrical and toroidal boundary conditions.

In section 3 we begin by recalling the results of Baxter [1] for $\kappa_\pm(z)$ and the subsequent analysis of Joyce [5] for the high density regime for the polynomial relation between z and $\kappa_+(z)$. For the low density regime we derive a new polynomial relation between z and $\kappa_-(z)$. Some details of the analysis of $\kappa_\pm(z)$ and the associated density $\rho_-(z)$ are presented in Appendix A and Appendix B.

In section 4 we compute transfer matrix eigenvalues and equimodular curves for the maximum eigenvalues for values of L_h as large as 30. We demonstrate the difference between the equimodular curves of the full transfer matrix and the equimodular curves for eigenvalues restricted to the sector $P = 0$. These equimodular curves are compared with the partition functions per site $\kappa_\pm(z)$.

In section 5 we present the results for partition function zeros for both toroidal and cylindrical boundary conditions for a variety of $L_h \times L_v$ lattices. For $L_h = L_v$ the largest sizes are 39×39 for cylindrical and 27×27 for toroidal boundary conditions. We compare the zeros with $\kappa_\pm(z)$ and with the equimodular eigenvalue curves of section 4 for both the cases $L_v = L_h$ and $L_v \gg L_h$ and we analyze the density of zeros on the negative z axis. We analyze the dependence of the approach as $L \to \infty$ of the endpoints $z_d(L)$ and $z_c(L)$ to z_d and z_c by means of finite size scaling and identify several correction to scaling exponents.

In section 6 we use our results to discuss the relation of the free energy on the positive real fugacity axis to the partition function in the full complex fugacity plane and some concluding remarks are made in section 7. A description of the methods used for the numerical computations of eigenvalues and zeros are given in Appendix E and the numerical details of the finite size scaling are given in Appendix F.

2. Preliminaries

In this section we review the concepts of partition function, transfer matrix, free energy and partition function zeros and highlight the properties we discuss in later sections.

2.1. Partition function

The hard hexagon model is defined on a triangular lattice, which is conveniently viewed as a square lattice with an added diagonal on each face as shown in figure 1. Particles are placed on the sites of the lattice with the restriction that if there is a particle at one site no particle is allowed at the six nearest neighbor sites. The grand canonical partition function on the lattice with L_v rows and L_h columns is computed as

$$Z_{L_v, L_h}(z) = \sum_{N=0}^{\infty} g(N) \cdot z^N, \tag{6}$$

where $g(N)$ is the number of allowed configurations with N particles. By definition on a finite lattice the partition function is a polynomial which can be described by its zeros z_k as $\prod (1 - z/z_k)$. For hard hexagons the order of the polynomial is bounded above by $L_v L_h/3$ which becomes an equality when it is an integer.

2.2. Transfer matrices

An alternative and quite different representation of the partition function on the finite lattice is given in terms of a transfer matrix $T(z; L_h)$ computed in terms of the local Boltzmann weights in figure 1 as

$$T_{\{b_1, \cdots b_{L_h}\}, \{a_1, \cdots a_{L_h}\}} = \prod_{j=1}^{L_h} W(a_j, a_{j+1}; b_j, b_{j+1}), \tag{7}$$

where the occupation numbers a_j and b_j take the values 0 and 1 and for periodic boundary conditions in the horizontal direction we use the convention that $L_h + 1 \equiv 1$. Then the hard hexagon weights $W(a_j, a_{j+1}; b_j, j_{j+1})$ are written (see page 403 of [2]) in the form

$$W(a_j, a_{j+1}; b_j, b_{j+1}) = 0$$
$$\text{for} \quad a_j a_{j+1} = b_j b_{j+1} = a_j b_j = a_{j+1} b_{j+1} = a_{j+1} b_j = 1, \tag{8}$$

and otherwise:

$$W(a_j, a_{j+1}; b_j, b_{j+1}) = z^{(a_j + a_{j+1} + b_j + b_{j+1})/4}. \qquad (9)$$

This transfer matrix does not satisfy $T = T^t$: thus there may be complex eigenvalues even for $z \geq 0$. As far as real values of z are concerned, the matrix elements are all non negative for $z \geq 0$ and, thus, by the Perron-Frobenius theorem the maximum eigenvalue is real and positive.
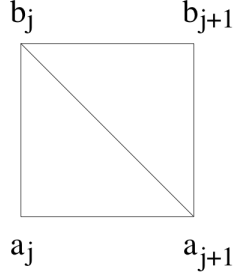
Figure 1. Boltzmann weights for the transfer matrix of hard hexagons

For lattices with toroidal boundary conditions where there are periodic boundary conditions in the vertical direction

$$Z^P_{L_v, L_h}(z) = \operatorname{Tr} T^{L_v}(z; L_h). \qquad (10)$$

For lattices with cylindrical boundary conditions where there are free boundary condition in the vertical direction

$$Z^C_{L_v, L_h}(z) = \langle \mathbf{v}_B | T^{L_v}(z; L_h) | \mathbf{v}'_B \rangle, \qquad (11)$$

where $\mathbf{v}_B$ and $\mathbf{v}'_B$ are suitable vectors for the boundary conditions on rows 1 and L_v. For the transfer matrix (7) with Boltzmann weights given by the symmetrical form (8) with (9) the components of the vectors $\mathbf{v}_B$ and $\mathbf{v}'_B$ for free boundary conditions are

$$\mathbf{v}_B(a_1, a_2, \cdots, a_{L_h}) = \mathbf{v}'_B(a_1, a_2, \cdots, a_{L_h}) = \prod_{j=1}^{L_h} z^{a_j/2}. \qquad (12)$$

When the transfer matrix is diagonalizable (10) and (11) may be written in terms of the eigenvalues λ_k and eigenvectors $\mathbf{v}_k$ of the transfer matrix $T_{L_h}(z)$ as

$$Z^P_{L_v, L_h}(z) = \sum_k \lambda_k^{L_v}(z; L_h) \qquad \text{and} \qquad (13)$$

$$Z^C_{L_v, L_h}(z) = \sum_k \lambda_k^{L_v}(z; L_h) \cdot c_k \quad \text{where} \quad c_k = (\mathbf{v_B} \cdot \mathbf{v_k})(\mathbf{v_k} \cdot \mathbf{v'_B}). \qquad (14)$$

2.3. The thermodynamic limit

For finite size systems the hard hexagon partition function is a polynomial and the transfer matrix eigenvalues are all algebraic functions. However, for physics we must study the thermodynamic limit where L_v, $L_h \to \infty$ and, because both the partition function and the transfer matrix eigenvalues diverge in this limit we consider instead of the partition function the free energy

$$-F/k_B T = \lim_{L_v, L_h \to \infty} (L_v L_h)^{-1} \cdot \ln Z_{L_v, L_h}(z). \qquad (15)$$

For real positive values of z this limit must be independent of the aspect ratio $0 < L_v/L_h < \infty$ for thermodynamics to be valid.

In terms of the transfer matrix representations of the partition function (13) and (14) we take the limit $L_v \to \infty$

$$\lim_{L_v \to \infty} L_v^{-1} \cdot \ln Z_{L_v,L_h}(z) \;=\; \ln \lambda_{\max}(z; L_h). \tag{16}$$

For the limiting free energy (15) to exist and be non zero it is required that

$$0 \;<\; \lim_{L_h \to \infty} L_h^{-1} \cdot \ln \lambda_{\max}(z; L_h) \;<\; \infty, \tag{17}$$

or, equivalently, that the partition function per site exists

$$\kappa(z) \;=\; \lim_{L_h \to \infty} \lambda_{\max}\left(z; L_h\right)^{1/L_h} \;<\; \infty, \tag{18}$$

(in other words the maximum eigenvalue must be exponential in L_h). This exponential behavior will guarantee that for real positive z

$$\lim_{L_h \to \infty} \lim_{L_v \to \infty} (L_v L_h)^{-1} \ln Z_{L_v,L_h}(z) \;=\; \lim_{L_v,L_h \to \infty} (L_v L_h)^{-1} \cdot \ln Z_{L_v,L_h}(z), \tag{19}$$

independent of the aspect ratio L_v/L_h. However for complex "nonphysical values" of z this independence of the ratio L_v/L_h is not obvious. In particular for hard squares at $z = -1$ *all* eigenvalues of the transfer matrix lie on the unit circle and the partition function $Z_{L_v,L_h}(-1)$ depends on number theoretic properties [6]-[9] of L_v and L_h.

2.4. Partition function zeros versus transfer matrix eigenvalues

It remains in this section to relate partition function zeros to transfer matrix eigenvalues and eigenvectors. For finite lattices the partition function zeros can be obtained from (13) and (14) if all eigenvalues and eigenfunctions are known. We begin with the simplest case where

$$L_v \;\to\; \infty \qquad \text{with fixed} \qquad L_h, \tag{20}$$

considered by Beraha, Kahane and Weiss [10]-[12] as presented by Salas and Sokal [13]. This is the case of a cylinder of infinite length with L_h sites in the finite direction where the aspect ratio $L_v/L_h \to \infty$.

Generically the eigenvalues have different moduli and in the limit (20) the partition function will have zeros when two or more maximum eigenvalues of $T(z; L_h)$ have equal moduli

$$|\lambda_1(z; L_h)| \;=\; |\lambda_2(z; L_h)|. \tag{21}$$

The locus in the complex plane z is called an equimodular curve [24]-[27]. On this curve

$$\frac{\lambda_1(z; L_h)}{\lambda_2(z; L_h)} \;=\; e^{i\phi(z)}, \tag{22}$$

where $\phi(z)$ is real and depends on z. The density of zeros on this curve is proportional to $d\phi(z)/dz$.

A simple example occurs for hard hexagons where on segments of the negative z-axis there is a complex conjugate pair of eigenvalues which have the maximum modulus.

However, we will see that for the hard hexagon model there are points in the complex plane where more than two eigenvalues values have equal moduli. Indeed, for

hard squares at $z = -1$, we have previously noted that all eigenvalues have modulus one.

For values of z in the complex plane where the interchange of (19) holds the limiting locus of partition function zeros for the square $L_v = L_h$ lattice will coincide with the transfer matrix equimodular curves. However there is no guarantee that the interchange (19) holds in the entire complex z plane.

Our considerations are somewhat different for toroidal and cylindrical boundary conditions and we treat these two cases separately.

2.4.1. Cylindrical boundary conditions For cylindrical boundary conditions the partition function is given by (14) which in addition to the eigenvalues of $T(L_h)$ depends on the boundary vector $\mathbf{v}_B$ (12). Because of the periodic boundary conditions in the L_h direction there is a conserved momentum P. Consequently the transfer matrix and translation operator may be simultaneously diagonalized. Therefore the transfer matrix may be block diagonalized by a transformation which is independent of z and hence the characteristic equation will factorize. Furthermore the boundary vector (12) for the cylindrical case satisfies

$$\mathbf{v}_B(a_1, a_2, \cdots, a_{L_h}) = \mathbf{v}_B(a_{L_h}, a_1, \cdots, a_{L_h-1}) \tag{23}$$

and thus is also translationally invariant. Therefore the only eigenvectors which contribute to the partition function in (14) lie in the translationally invariant subspace where $P = 0$. Consequently we are able to restrict our attention to the reduced transfer matrix for this translationally invariant sector where the momentum of the state is $P = 0$ because all of the scalar products c_k in (14) for eigenvectors in sectors with $P \neq 0$ vanish.

2.4.2. Toroidal boundary conditions

For toroidal boundary conditions the partition function in (13) is the sum over all eigenvalues and a new feature arises because for $P \neq 0, \pi$ the eigenvalues for $\pm P$ are degenerate in modulus, but may have complex conjugate phases which are independent of z. By grouping these two eigenvalues together we see that the discussion leading to (21) still applies. There are now three types of equimodular curves:

    1) Two eigenvalues are equal for crossings of eigenvectors with $P = 0, \pi$,

    2) Three eigenvalues are equal for crossings of eigenvectors of $P = 0, \pi$ with $P \neq 0, \pi$,

    3) Four eigenvalues are equal for crossing of eigenvectors with $P \neq 0, \pi$.

2.4.3. Nonzero finite aspect ratios L_v/L_h

We are, of course, not really interested in the limit (20) but rather in the case of finite nonzero aspect ratio L_v/L_h and particularly in the isotropic case $L_v = L_h$. There is apparently no general theory for finite nonzero aspect ratio in the literature and we will study this case in detail below.

3. The partition functions $\kappa_\pm(z)$ per site for hard hexagons

Baxter [1, 2] has computed the fugacity and the partition function per site in terms of an auxiliary variable x using the functions

$$G(x) = \prod_{n=1}^{\infty} \frac{1}{(1 - x^{5n-4})(1 - x^{5n-1})}, \tag{24}$$

$$H(x) = \prod_{n=1}^{\infty} \frac{1}{(1 - x^{5n-3})(1 - x^{5n-2})}, \qquad Q(x) = \prod_{n=1}^{\infty} (1 - x^n). \tag{25}$$

For high density where $0 < z^{-1} < z_c^{-1}$ the results are

$$z = \frac{1}{x} \cdot \left(\frac{G(x)}{H(x)} \right)^5 \qquad \text{and} \tag{26}$$

$$\kappa_+ = \frac{1}{x^{1/3}} \cdot \frac{G^3(x)\,Q^2(x^5)}{H^2(x)} \cdot \prod_{n=1}^{\infty} \frac{(1 - x^{3n-2})(1 - x^{3n-1})}{(1 - x^{3n})^2}, \tag{27}$$

where, as x increases from 0 to 1, the value of z^{-1} increases from 0 to z_c^{-1}.

For low density where $0 \le z < z_c$

$$z = -x \cdot \left(\frac{H(x)}{G(x)} \right)^5 \qquad \text{and} \tag{28}$$

$$\kappa_- = \frac{H^3(x)\,Q^2(x^5)}{G^2(x)} \cdot \prod_{n=1}^{\infty} \frac{(1 - x^{6n-4})(1 - x^{6n-3})^2(1 - x^{6n-2})}{(1 - x^{6n-5})(1 - x^{6n-1})(1 - x^{6n})^2}, \tag{29}$$

where, as x decreases from 0 to -1, the value of z increases from 0 to z_c.

3.1. Algebraic equations for $\kappa_\pm(z)$

The auxiliary variable x can be eliminated between the expressions for z and κ (26)-(29) and the resulting functions $\kappa_\pm(z)$ are in fact algebraic functions of z. To give these algebraic equations we follow Joyce [5] and introduce the functions

$$\begin{align}
\Omega_1(z) &= 1 + 11z - z^2, \tag{30}\\
\Omega_2(z) &= z^4 + 228z^3 + 494z^2 - 228z + 1, \tag{31}\\
\Omega_3(z) &= (z^2 + 1) \cdot (z^4 - 522z^3 - 10006z^2 + 522z + 1). \tag{32}
\end{align}$$

For the high density Joyce (see eqn. (7.9) in [5]) showed that the function $\kappa_+(z)$ satisfies a polynomial relation of degree 24 in the variable $\kappa_+(z)$

$$f_+(z, \kappa_+) = \sum_{k=0}^{4} C_k^+(z) \cdot \kappa_+^{6k} = 0, \qquad \text{where} \tag{33}$$

$$\begin{align}
C_0^+(z) &= -3^{27}\,z^{22}\\
C_1^+(z) &= -3^{19}\,z^{16} \cdot \Omega_3(z),\\
C_2^+(z) &= -3^{10}\,z^{10} \cdot [\Omega_3^2(z) - 2430\,z \cdot \Omega_1^5(z)],\\
C_3^+(z) &= -z^4 \cdot \Omega_3(z) \cdot [\Omega_3^2(z) - 1458\,z \cdot \Omega_1^5(z)]\\
C_4^+(z) &= \Omega_1^{10}(z). \tag{34}
\end{align}$$

Joyce has also derived an algebraic equation for the density (see eqn. (8.28) in [5]) which follows from (33).

For low density we have obtained by means of a Maple computation the substantially more complicated polynomial relation which was not obtained in [5]

$$f_-(z, \kappa_-) \;=\; \sum_{k=0}^{12} C_k^-(z) \cdot \kappa_-^{2k} \;=\; 0, \qquad\qquad \text{where} \qquad\qquad (35)$$

$$
\begin{aligned}
C_0^-(z) &= -2^{32} \cdot 3^{27} \cdot z^{22}, \\
C_1^-(z) &= 0 \\
C_2^-(z) &= 2^{26} \cdot 3^{23} \cdot 31 \cdot z^{18} \cdot \Omega_2(z), \\
C_3^-(z) &= 2^{26} \cdot 3^{19} \cdot 47 \cdot z^{16} \cdot \Omega_3(z), \\
C_4^-(z) &= -2^{17} \cdot 3^{18} \cdot 5701 \cdot z^{14} \cdot \Omega_2^2(z), \\
C_5^-(z) &= -2^{16} \cdot 3^{14} \cdot 7^2 \cdot 19 \cdot 37 \cdot z^{12} \cdot \Omega_2(z)\,\Omega_3(z), \\
C_6^-(z) &= -2^{10} \cdot 3^{10} \cdot 7 \cdot z^{10} \cdot [273001 \cdot \Omega_3^2(z) + 2^6 \cdot 3^5 \cdot 5 \cdot 4933 \cdot z \cdot \Omega_1^5(z)], \\
C_7^-(z) &= -2^9 \cdot 3^{10} \cdot 11 \cdot 13 \cdot 139 \cdot z^8 \cdot \Omega_3(z)\,\Omega_2^2(z), \\
C_8^-(z) &= -3^5 \cdot z^6 \cdot \Omega_2(z) \cdot [7 \cdot 1028327 \cdot \Omega_3^2(z) - 2^6 \cdot 3^4 \cdot 11 \cdot 419 \cdot 16811 \cdot z \cdot \Omega_1^5(z)], \\
C_9^-(z) &= -z^4 \cdot \Omega_3(z) \cdot [37 \cdot 79087\,\Omega_3^2(z) + 2^6 \cdot 3^6 \cdot 5150251 \cdot z \cdot \Omega_1^5(z)], \\
C_{10}^-(z) &= -z^2 \cdot \Omega_2^2(z) \cdot [19 \cdot 139\Omega_3^2(z) - 2 \cdot 3^6 \cdot 151 \cdot 317 \cdot z \cdot \Omega_1^5(z)] \\
C_{11}^-(z) &= -\Omega_2(z)\,\Omega_3(z) \cdot [\Omega_3^2(z) - 2 \cdot 613 \cdot z \cdot \Omega_1^5(z)], \\
C_{12}^-(z) &= \Omega_1^{10}(z).
\end{aligned}
\qquad (36)
$$

We have verified that Joyce's algebraic equation for the density (see eqn. (12.10) in [5]) follows from (35).

We note the symmetry

$$z^{44} \cdot f_\pm\left(-\frac{1}{z}, \frac{\kappa_\pm}{z}\right) \;=\; f_\pm(z, \kappa). \qquad (37)$$

In Appendix A we discuss the behavior $\kappa_\pm(z)$ at the singular points $z_c, \; z_d$.

3.2. Partition function for complex z

From section 2.4 we see that the simplest construction of the partition function of hard hexagons in the complex z plane would be if the low and high density eigenvalues in the thermodynamic limit were the only two eigenvalues of maximum modulus and that the interchange of limits (19) holds for z in the entire complex plane. Then the zeros would be given by the equimodular curve $|\kappa_+(z)| = |\kappa_-(z)|$. Because the partition functions per site $\kappa_\pm(z)$ satisfy algebraic equations this curve will satisfy an algebraic equation which can be found by setting $\kappa_+(z) = r\kappa_-(z)$ in the equation (33) for $\kappa_+(z)$ and computing the resultant between equations (35) and (33). The solutions of this equation for r on the unit circle will give all the locations where $\kappa_\pm(z)$ have equimodular solutions. We have produced this equation using Maple but unfortunately is it too large to print out. However, we are only interested in the crossings of the maximum modulus eigenvalues. Consequently we have computed this curve not from its algebraic equation but directly from the parametric representations (26)-(29). We plot this curve in figure 2. The curve crosses the positive real axis at z_c and the negative real axis at $z = -5.9425104 \cdots$ which is exactly determined from

the algebraic equation of the equimodular curve given in Appendix C. The tangent to the equimodular curve is discontinuous at this negative value of z.

We will see in the next section that this two eigenvalue assumption is insufficient to account for our finite size computations in some regions of the plane.
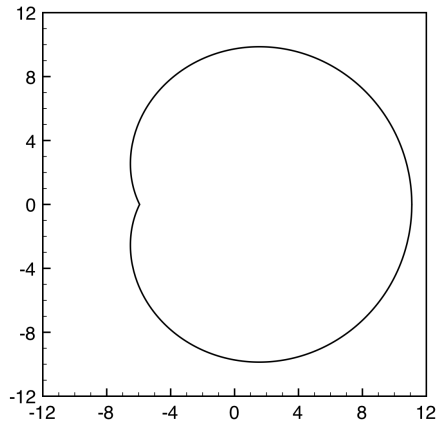
Figure 2. The equimodular curve for $|\kappa_-(z)| = |\kappa_+(z)|$ in the complex z plane. The crossing of the positive z axis is at z_c and the crossing of the negative z axis is at $z = -5.925104\cdots$

4. Transfer matrix eigenvalues

To obtain further information on the partition function in the complex z plane we compute, in this section, the eigenvalues for finite sizes of the transfer matrix $T(z; L_h)$ for the case of periodic boundary conditions in the L_h direction.

There are two ways to study the eigenvalues of the transfer matrix; analytically and numerically. Numerical computations can be carried out on matrices which are too large for symbolic computer programs to handle. However, analytic computations reveal properties which cannot be seen in numerical computations. Consequently we begin our presentation with analytic results before we present our numerical results.

4.1. Analytic results

The eigenvalues of a matrix are obtained as the solutions of its characteristic equation. For the transfer matrices of the hard hexagon model this characteristic equation is a polynomial in the parameter z and the eigenvalue λ with integer coefficients. Consequently the eigenvalues λ are algebraic functions of z. In general such characteristic polynomials will be irreducible (i.e. they will not factorize into products of polynomials with integer coefficients).

There are two important analytic non-generic features of the hard hexagon eigenvalues: factorization of the characteristic equation and the multiplicity of the roots of the resultant.

4.1.1. Factorization of the characteristic equation
For a transfer matrix with cylindrical boundary conditions the characteristic equation factorizes into subspaces characterized by a momentum eigenvalue P. In

general the characteristic polynomial in the translationally invariant $P = 0$ subspace will be irreducible. We have found that this is indeed the case for hard squares. However, for hard hexagons we find that for $L_h = 12, 15, 18$, the characteristic polynomial, for $P = 0$, factors into the product of two irreducible polynomials with integer coefficients. We have not been able to study the factorization for larger values of L_h but we presume that factorization always occurs and is a result of the integrability of hard hexagons. What is unclear is if for larger lattices a factorization into more than two factors can occur.

4.1.2. Multiplicity of the roots of the resultant

An even more striking non-generic property of hard hexagons is seen in the computation of the resultant of the characteristic polynomial in the translationally invariant sector. The zeros of the resultant locate the positions of all potential singularities of the solutions of the polynomials.

We have been able to compute the resultant for $L_h = 12, 15, 18$, and find that almost all zeros of the resultant have multiplicity two which indicates that there is in fact no singularity at those points and that the two eigenvalues cross. This very dramatic property will almost certainly hold for all L_h and must be a consequence of the integrability (although to our knowledge no such theorem is in the literature).

4.2. Numerical results in the sector $P = 0$

For the partition function with cylindrical boundary conditions only the transfer matrix eigenvalues with $P = 0$ contribute. In this sector we have numerically computed eigenvalues of the transfer matrix, in the $P = 0$ sector, for systems of size as large as $L_h = 30$ which has dimension 31836. For such large matrices brute force computations will obviously not be sufficient and we have developed algorithms specific to this problem which we sketch in Appendix E. We restrict our attention to values of L_h being a multiple of three, to minimize boundary effects which will occur when the circumference L_h is incompatible with the three-sublattice structure of the triangular lattice.

In figure 3 we plot the equimodular curves for the crossing of the largest transfer matrix eigenvalues in the $P = 0$ sector for $L_h = 12, 15, 18, 21, 24, 27$, and in figure 4 we plot $L_h = 30$. It is obvious from these curves that more than two eigenvalues of the transfer matrix contribute to the partition function because of the increasing number of regions in the left half plane which we refer to as the "necklace". A striking feature is that there is a pronounced mod 6 effect where for $L_h \equiv 3 \pmod 6$ there is a level crossing curve in the necklace on the negative real z axis which is not present for $L_h \equiv 0 \pmod 6$. The level crossing curves separate the necklace into well defined regions. The number of these regions is $L_h/3 - 4$ for $L \leq 27$. The number of regions for $L_h = 30$ is the same as for $L_h = 24$. For $L_h = 21, 27$ all the branch points of the necklace are given in table 1 and in table 2 for $L_h = 18, 24, 30$.

There are further features in figures 3 and 4 which deserve a more detailed discussion.

4.2.1. Comparison with the equimodular curve of $\kappa_\pm(z)$

If the two eigenvalues $\kappa_\pm(z)$ computed in [1] were sufficient to describe the $L_h \to \infty$ thermodynamic limit of these finite size computations then the equimodular curves of

figures 3 and 4 must approach the equimodular curve of $\kappa_\pm(z)$ of figure 2. We make this comparison for $L_h = 30$ in figure 4.

In figure 4 the agreement of the $\kappa_\pm(z)$ level crossing curve with the eigenvalue equimodular curve for $L_h = 30$ is exceedingly good in the entire portion of the plane which does not include the necklace. However, in the necklace region the $\kappa_\pm(z)$ curve does not agree with either the inner or outer boundaries of the necklace but rather splits the necklace region into two parts.

A more quantitative argument follows from the values of the leftmost crossing with the negative real axis of the necklace given in table 1 for $L_h \equiv 0 \pmod 6$ and in table 2 for $L_h \equiv 3 \pmod 6$. In both cases the left most crossing moves to the left to a value which if extrapolate in terms of $1/L_h$ lies between 9 and 10. The Y branching in tables 1 and 2 also moves to the left but does not extrapolate to a value to the left of $z = -5.9425104\cdots$ where the $\kappa_\pm(z)$ equimodular curve crosses the negative real axis. We interpret this as implying that the necklace persists in the thermodynamic limit and that at least one more transfer matrix eigenvalue is needed to explain the analyticity of the free energy in the complex z plane.

$L_h = 21$	$L_h = 27$	comment
-3.7731	-4.1138	Y branching
$-5.5898 \pm 5.8764i$	$-4.6228 \pm 7.2480i$	necklace end
	$-5.2737 \pm 6.5159i$	
	$-5.2321 \pm 6.3840i$	
$-5.2264 \pm 1.3949i$	$-5.3175 \pm 1.4134i$	
$-7.2883 \pm 2.4533i$	$-7.6848 \pm 2.4225i$	
-7.9020	-8.2803	leftmost crossing

Table 1. The branch points of the necklace of the equimodular curves of hard hexagons with cylindrical boundary conditions for $L_h = 21, 27$.

$L_h = 18$	$L_h = 24$	$L_h = 30$	comment
-3.8370	-4.0637	-4.3794	Y branching
$-6.3703 \pm 4.0485i$	$-4.8079 \pm 7.0090i$	$-4.4043 \pm 7.4623i$	necklace end
	$-6.5389 \pm 4.7519i$	$-6.9134 \pm 4.4771i$	
	$-5.8477 \pm 3.8460i$	$-5.8526 \pm 3.4864i$	
-7.1499	-7.8663	-8.0937	leftmost crossing

Table 2. The branch points of the necklace of the equimodular curves of hard hexagons with cylindrical boundary conditions for $L_h = 18, 24, 30$.

4.2.2. The endpoints $z_d(L_h)$ and $z_c(L_h)$

In table 3 we give the endpoints which approach the unphysical and the physical singular points of the free energy z_d and z_c. We also give in this table the ratio of the largest to the next largest eigenvalue at $z_d(L_h)$ and $z_c(L_h)$ as determined from eigenvalue crossings. In the limit $L_h \to \infty$ this ratio must go to unity so the deviation from one is a measure of how far the finite size L_h is from the thermodynamic limit.
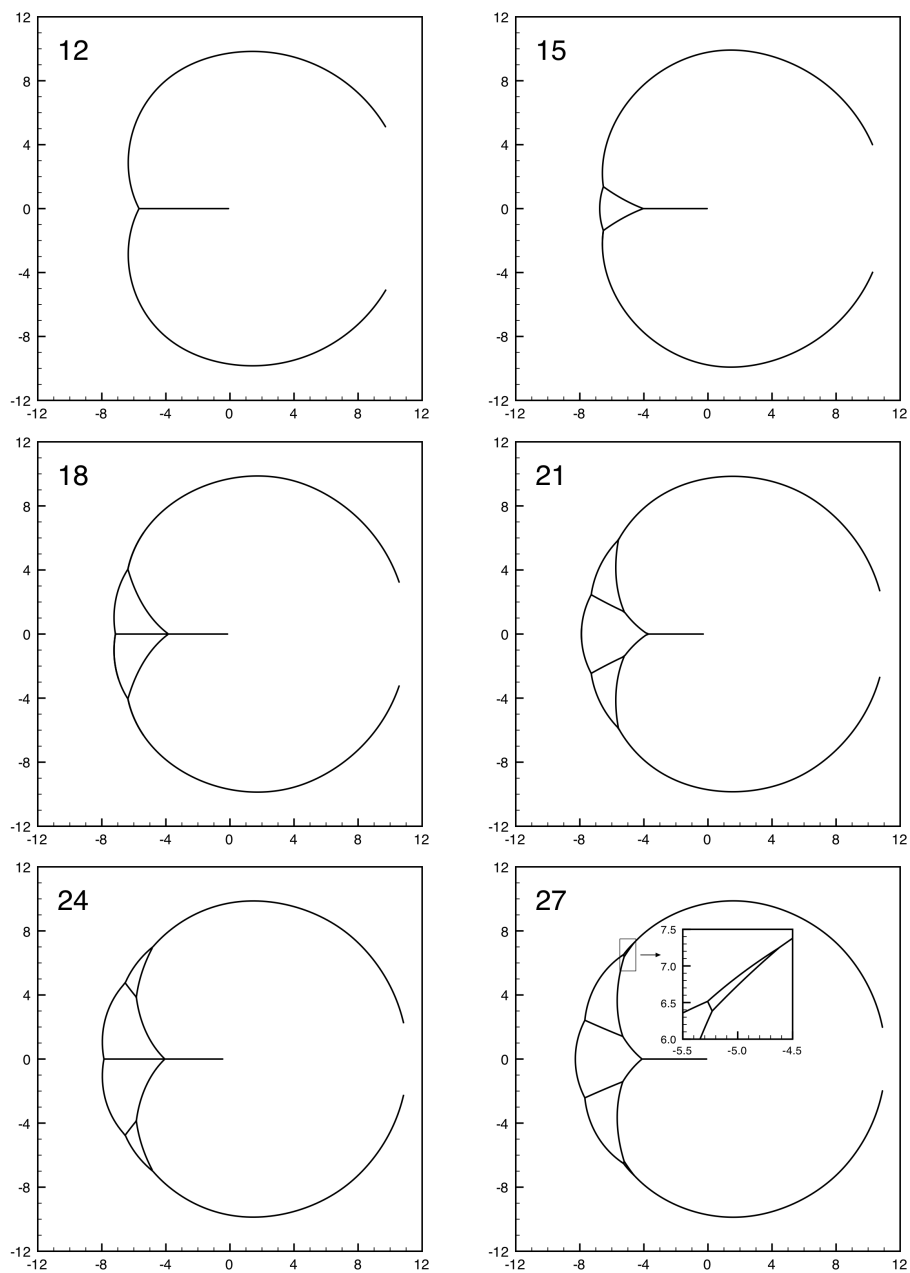
Figure 3. Plots in the complex fugacity plane z of the equimodular curves of hard hexagon eigenvalues with cylindrical boundary conditions of size $L_h = 12, 15, 18, 21, 24, 27$. The value of L_h is given in the upper left hand corner of the plots.
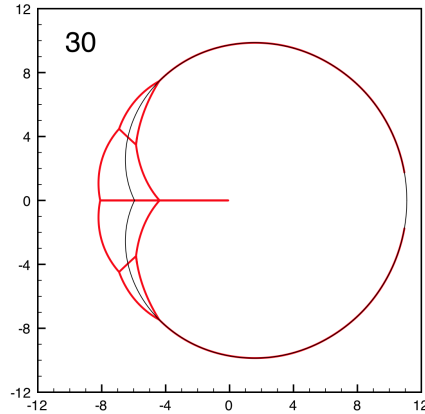
Figure 4. Comparison of the dominant eigenvalue crossings $L_h = 30$ shown in red with the equimodular curve $|\kappa_+(z)| = |\kappa_-(z)|$ of figure 2 shown in black. Color online.

L_h	$z_d(L_h)$	$\lambda_1/\lambda_{\max}$	$z_c(L_h)$	$\lambda_1/\lambda_{\max}$
12	-0.09051765	0.45085	$9.7432 \pm 5.0712i$	0.55487
15	-0.09037303	0.53048	$10.2971 \pm 3.9465i$	0.54278
18	-0.09030007	0.59046	$10.5753 \pm 3.2016i$	0.58463
21	-0.09026034	0.63709	$10.7340 \pm 2.6730i$	0.62006
24	-0.09023555	0.67431	$10.8310 \pm 2.2852i$	0.65030
27	-0.09021968	0.70467	$10.8955 \pm 1.9834i$	0.67582
30	-0.09020833	0.72989	$10.9389 \pm 1.7499i$	0.69827
∞	-0.09016994	1.00000	11.09016994	1.00000

Table 3. The values of the endpoints $z_d(L)$, $z_c(L)$ for hard hexagons on the cylindrical lattice with length L_h as determined from the equimodular eigenvalue curves and the ratios of the first excited state λ_1 to the largest eigenvalue $\lambda_{\max}$ at $z_d(L_h)$ and $z_c(L_h)$.

4.3. Eigenvalues for the toroidal lattice partition function

For lattices with toroidal boundary conditions the eigenvalues of all momentum sectors, not just $P = 0$, contribute to the partition function. In particular, in the thermodynamic limit for $P = \pm 2\pi/3$, it is shown in [14] that there is an eigenvalue $\lambda_{\pm 2\pi/3}(z; L_h)$ such that for $z \geq z_c$

$$\lim_{L_h \to \infty} \frac{\lambda_{\pm 2\pi/3}(z; L_h)}{\lambda_{\max}(z; L_h)} = e^{\pm 2\pi i/3}. \tag{38}$$

These two eigenvalues with $P = \pm 2\pi/3$ cause significant differences from the equimodular curves for $P = 0$ for finite values of L_h. We illustrate this in figures 5 and 6. In figure 5 we plot the equimodular curves for toroidal boundary conditions for $L_h = 9, 12, 15, 18, 21$.

In these figures level crossings of 2 eigenvalues are shown in red, of 3 eigenvalues in green and 4 eigenvalues in blue. For sectors separated by a red boundary, both

sectors have momentum $P = 0$. For sectors separated by a green boundary, one sector has momentum $P = 0$, and the other has two eigenvalues of equal modulus and fixed phases of $e^{\pm 2\pi i/3}$. For sectors separated by a blue boundary, each sector has two eigenvalues of equal modulus, and fixed phases of $e^{\pm 2\pi i/3}$. The equimodular curve $|\kappa_-(z)| = |\kappa_+(z)|$ is plotted in black for comparison.

It is instructive to compare the necklace regions of the plots of figure 5 with the corresponding plots of figure 3 where the momentum of the eigenvalues is restricted to $P = 0$. We do this in figure 6 where in the necklace region we have added in dotted red lines the $P = 0$ level crossing of figure 3 which are, now, crossings of sub-dominant eigenvalues.

There are two important observations to make concerning these plots.

4.3.1. The rays out to infinity

The most striking difference between the equimodular curves for cylindrical and toroidal boundary conditions is that there are "rays" of equimodular curves which go to infinity. These rays all have three equimodular eigenvalues which separate a sector
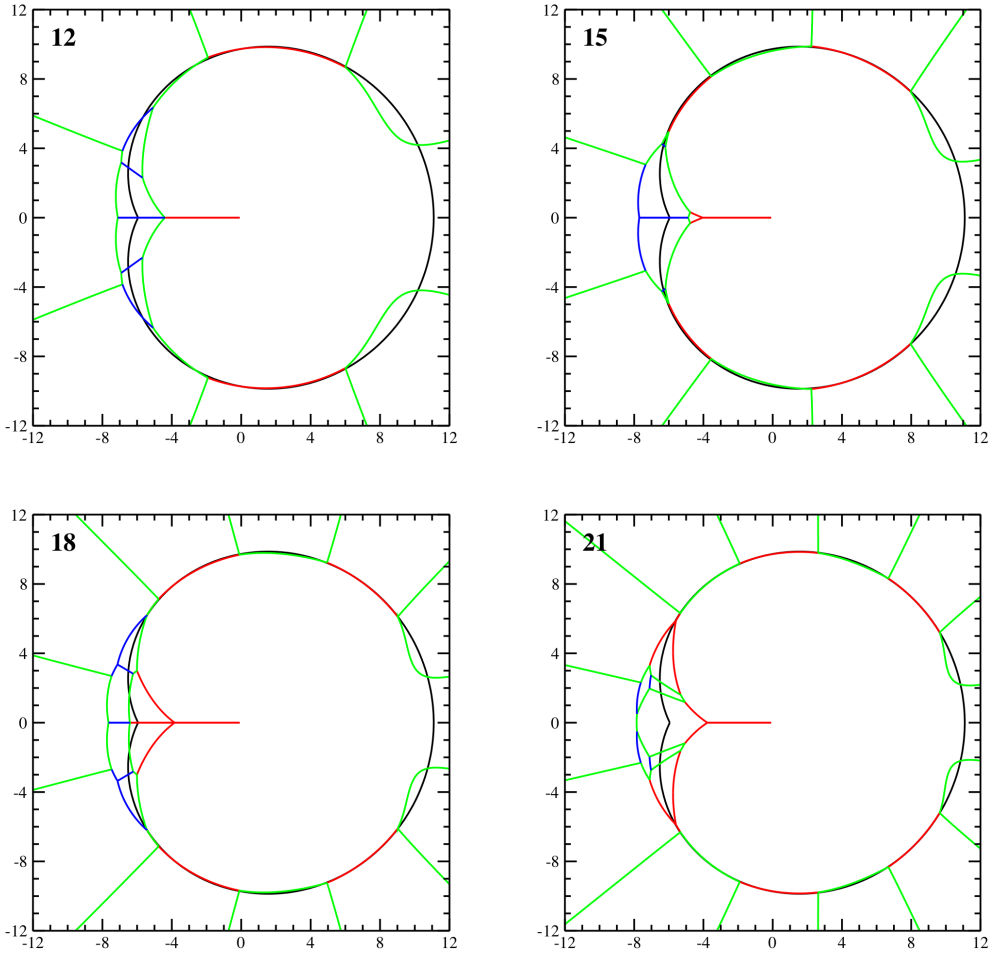
Figure 5. Plots in the complex fugacity plane z of the equimodular curves of hard hexagon eigenvalues for toroidal lattices for $L = 12, 15, 18, 21$. On the red lines 2 eigenvalues are equimodular, on the green lines 3 eigenvalues are equimodular and on the blue lines 4 eigenvalues are equimodular. The equimodular curve $|\kappa_-(z)| = |\kappa_+(z)|$ is given in black for comparison. Color online.

with $P = 0$ from a sector with $P = \pm 2\pi/3$. In the limit $L_h \to \infty$ these three eigenvalues on the rays become equimodular independent of z, and thus there will be no zeros on these rays in the thermodynamic limit.

4.3.2. Dominance of $P = 0$ as $L_h \to \infty$

We see in figure 6 that for the smaller values of L_h, such as 12 and 15, a sizable portion the region in the necklace has momentum $P = \pm 2\pi/3$. However, as seen in the plots for $L_h = 18$, 21 and 24 as L_h increases the regions with $P = 0$ grow and squeeze the regions with $P = \pm 2\pi/3$ down to a very small area. It is thus most natural to conjecture that, in the limit $L_h \to \infty$, only momentum $P = 0$ survives,
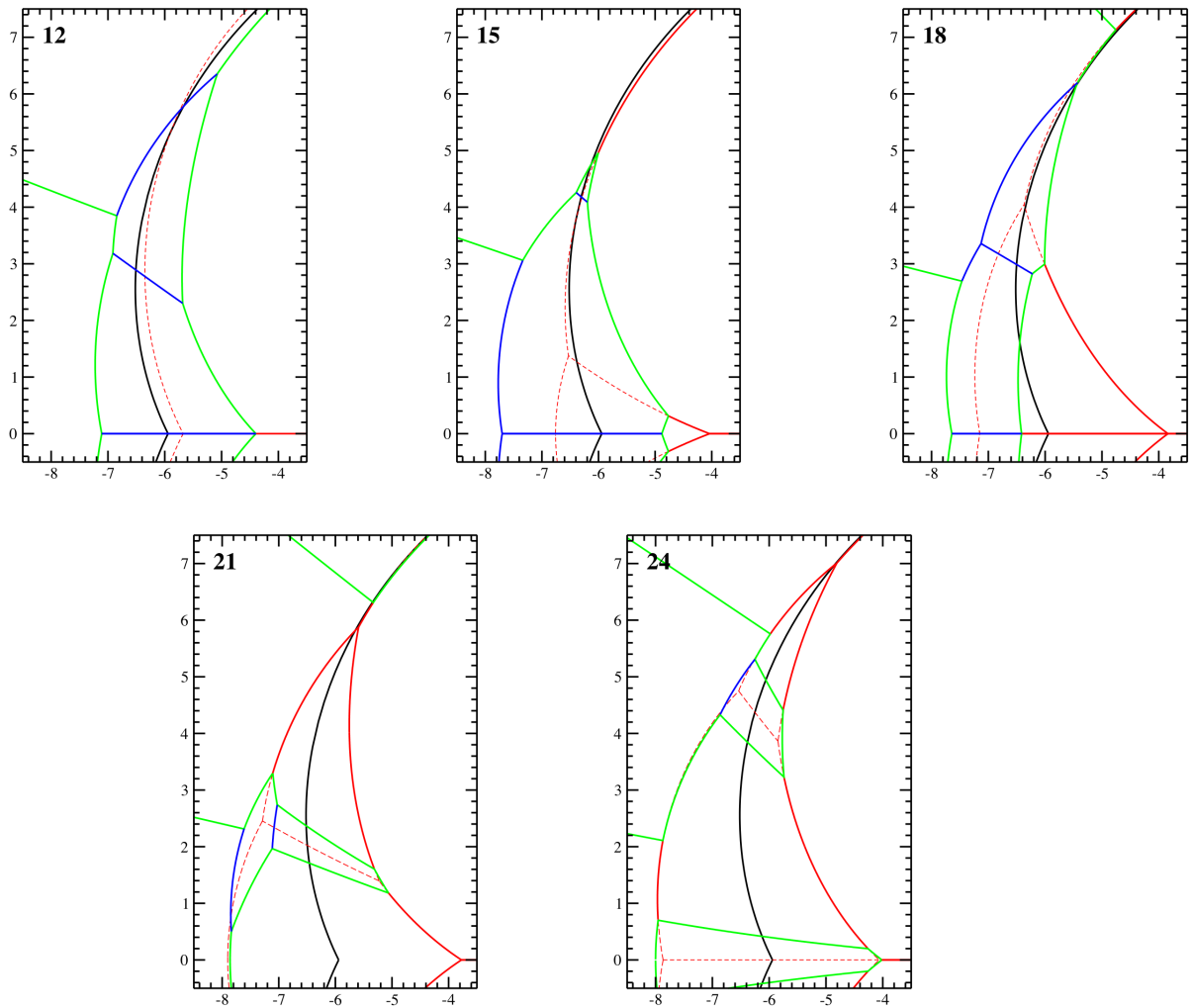
Figure 6. Comparison in the complex fugacity plane z of the necklace region of the equimodular curves of hard hexagon maximal eigenvalues for toroidal lattices for $L_h = 12$, 15, 18, 21, 24 with the eigenvalue crossing in the $P = 0$ sector of figure 3. On the red lines 2 eigenvalues are equimodular, on the green lines 3 eigenvalues are equimodular and on the blue lines 4 eigenvalues are equimodular. The dotted red curves are the additional crossings in the $P = 0$ sector from figure 3 which are now sub-dominant. The equimodular curve $|\kappa_-(z)| = |\kappa_+(z)|$ is given in black for comparison. Color online.

except possibly on the equimodular curves themselves.

5. Partition function zeros

We now turn to zeros of the partition function $Z_{L,L}(z)$ on the lattices of size $L \times L$. Just as we required the creation of specialized algorithms to compute the eigenvalues of the transfer matrix so we need specialized algorithms to compute the polynomials. We have studied both cylindrical and toroidal boundary conditions.

5.1. Cylindrical boundary conditions

We have computed partition function zeros for lattices with cylindrical boundary conditions for sizes up to 39×39. We plot these zeros in figure 7. These plots share with the equimodular $P = 0$ eigenvalue curves of figure 3 the feature of having a necklace in the left half plane beyond the Y branching. These plots also have the feature that as the size increases the number of zeros inside the necklace region increases. However, in contrast with the equimodular $P = 0$ eigenvalue curves there is no necklace for $L = 15$.

5.1.1. Branching of the necklace

We give the left most crossing of the necklace, the Y branching point and the necklace endpoint in table 4. We note that the left most crossing is to the left of the corresponding left most crossing of the transfer matrix eigenvalue equimodular crossings given in tables 1 and 2. These crossings are moving to the right with increasing L for $L \geq 27$. The Y branchings are moving to the right for $L \geq 30$. These trends are the opposite of what was found for the transfer matrix eigenvalue curves which only went up to $L_h = 27$. We note that for 15×15 through 27×27 there is only one region in the necklace. However. for 30×30 there are two regions, for 33×33 three, for 36×36 five and for 39×39 seven. It is unknown if the number of regions increases for larger lattices.

L	leftmost crossing	Y branching	necklace endpoints
15	no necklace	-6.8311	
18	-8.666	-5.6655	
21	-9.1957	-4.5411 (min)	
24	$-8.8963 \pm 0.264i$	-4.7137	
27	-9.4969	-4.8031	$-6.292287 \pm 7.325196i$
30	$-9.2717 \pm 0.541i$	-5.0851 (max)	$-5.515958 \pm 8.174231i$
33	-9.4610	-4.8875	$-4.728011 \pm 8.742729i$
36	$-9.213 \pm 0.527i$	-4.6972	$-4.797746 \pm 8.473961i$
39	-9.3221	-4.5687	$-4.270164 \pm 8.792602i$

Table 4. The necklace crossing and endpoints as a function of L for the $L \times L$ lattice with cylindrical boundary conditions. There is a mod 6 phenomenon apparent in both the location of the necklace crossings and the endpoint. The necklace endpoints at $L = 27$, 33, 39 and at $L = 30$, 36 are moving to the right.

5.1.2. Comparison with the eqimodular curves

In figure 8 we compare the equimodular curves for $L_h = 27$ with the partition function zeros of the 27×27 lattice by plotting the partition function zeros for the

lattices 27×27, 27×54, 27×135 and 27×270. This comparison clearly shows how slight kinks for 27×27 grow into an equimodular curve with 5 separate regions.
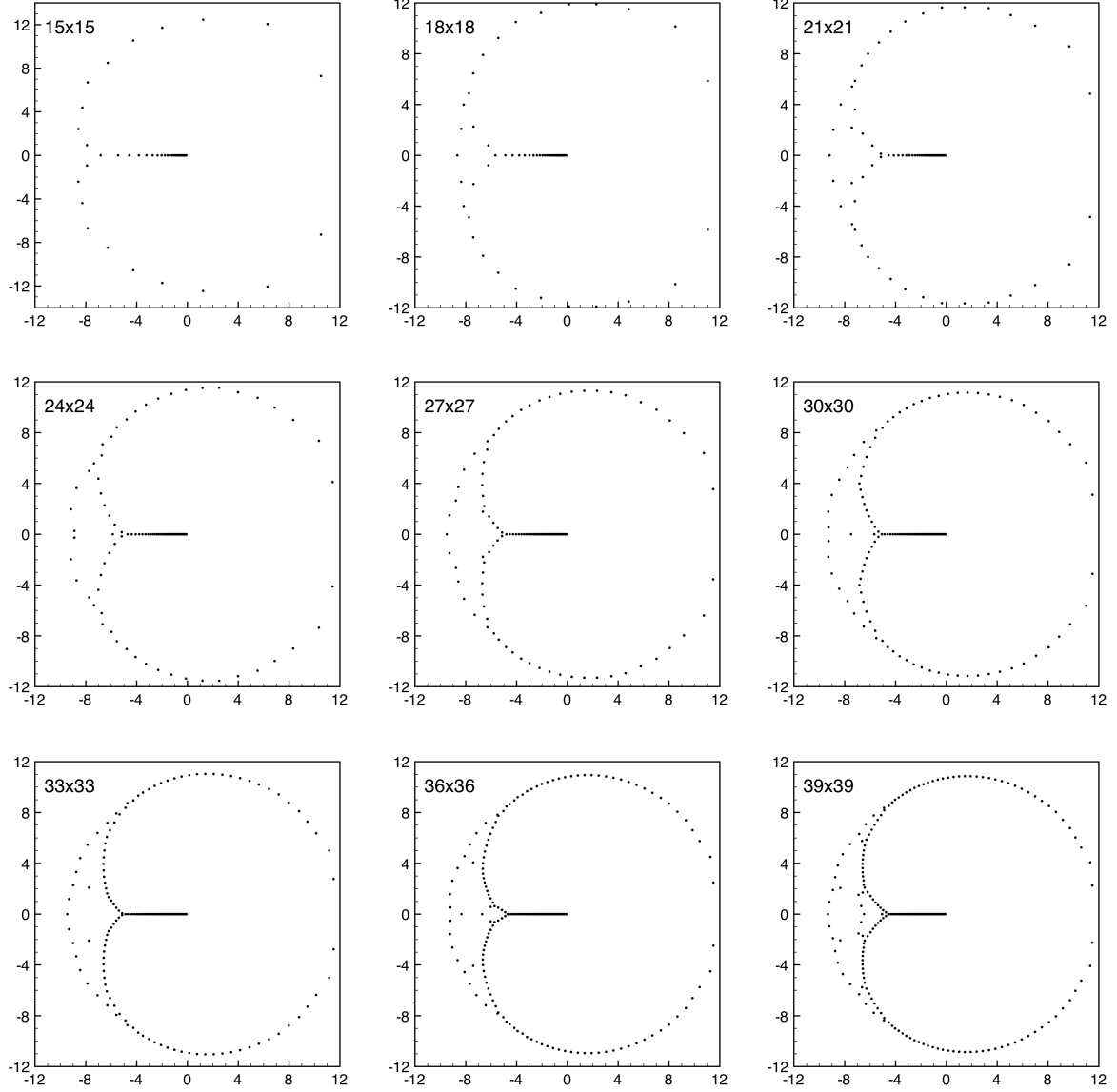
Figure 7. Plots of partition function zeros in the complex fugacity plane z of hard hexagon model for lattices with cylindrical boundary conditions of size 15×15, 18×18, 21×21, 24×24, 27×27, 30×30, 33×33, 36×36, 39×39.

5.1.3. The endpoints $z_d(L)$ and $z_c(L)$

In table 5 we give the values of the endpoints which approach z_d and z_c. We note that
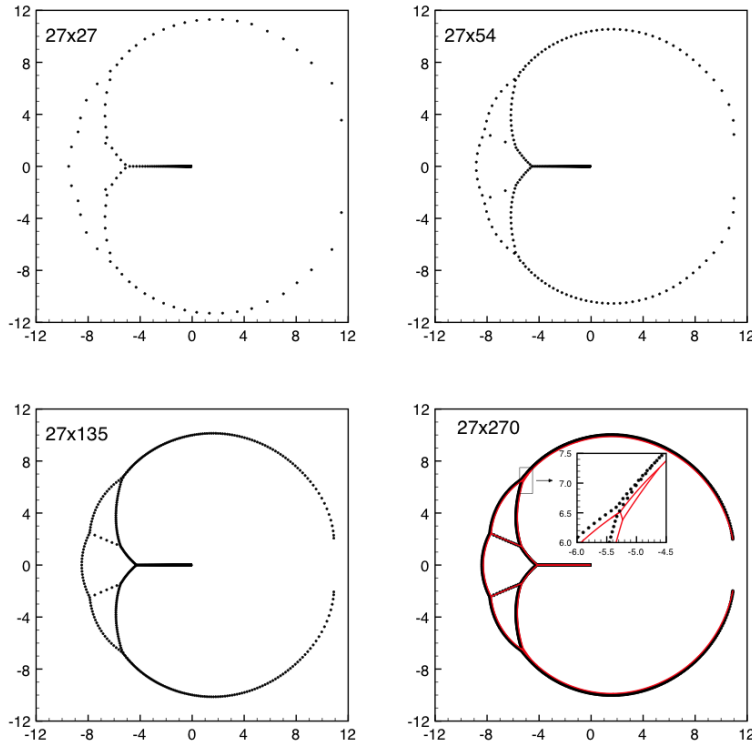
Figure 8. The partition function zeros for the lattices 27×27, 27×54 27×135 and 27×270. For 27×270 the equimodular curve is shown in red. Color online

the values of $z_d(L_h)$ and $z_c(L_h)$ of table 3 as determined from the equimodular curves are significantly closer to the limiting values z_d and z_c than the corresponding values of table 5. We also note that, in table 3, $\mathrm{Re}(z_c(L_h))$ is monotonic and approaches z_c from below, while in table 5 $\mathrm{Re}(z_c(L_h))$ is not monotonic and approaches z_c from above.

It is clear in table 5 that $z_d(L)$ is converging rapidly to z_d and a careful quantitative analysis well fits the data with the form

$$z_d(L) - z_d = b_0 L^{-12/5} + b_1 L^{-17/5} + b_2 L^{-22/5} + a_3 L^{-27/5} + \cdots \tag{39}$$

with

$$b_0 = 1.7147(1), \quad b_1 = -9.30(2), \quad b_2 = 48(2), \quad b_3 = -180(30). \tag{40}$$

The exponent $12/5$ is the leading exponent of the energy operator of the Lee-Yang edge as is seen from analysis of [15] and [16]. It is expected to be the inverse of the correlation exponent ν at $z = z_d$ but a computation of this correlation length is not in the literature.

For $z_c(L)$ the data of table 5 is well fit by

$$|z_c(L)| - z_c = a_0 L^{-6/5} + a_1 L^{-2} + a_2 L^{-14/5} + \cdots \tag{41}$$

L	$z_d(L)$	$z_c(L)$
9	-0.0957417573	$5.9002937473 \pm 12.2312152474i$
12	-0.0932266680	$9.2335210855 \pm 9.3476347389i$
15	-0.0920714392	$10.5114514245 \pm 7.2812520022i$
18	-0.0914523473	$11.0571925423 \pm 5.8559364459i$
21	-0.0910853230	$11.3084528958 \pm 4.8492670401i$
24	-0.0908515103	$11.4268383658 \pm 4.1113758041i$
27	-0.0906942824	$11.4806273673 \pm 3.5521968857i$
30	-0.0905839894	$11.5012919280 \pm 3.1162734906i$
33	-0.0905039451	$11.5044258314 \pm 2.7682753249i$
36	-0.0904442058	$11.4981796564 \pm 2.4848695493i$
39	-0.0903985638	$11.4869896404 \pm 2.2501329582i$
∞	-0.0901699437	11.0901699437

Table 5. The values of $z_d(L)$, and $z_c(L)$ as a function of L for the $L \times L$ lattice with cylindrical boundary conditions as determined from the zeros of the partition function.

where

$$a_0 = 53.0(1), \quad a_1 = -50(5), \quad a_2 = -200(50) \tag{42}$$

where the exponent $y = 6/5$ is the inverse of the correlation length exponent ν of the hard hexagon model at $z = z_c$ [14]. The exponent -2 is consistent with $-y - |y'|$ where $y' = -4/5$ is the exponent for the subdominant energy operator $\phi_{(3.1)}$ for the three state Potts model [17] and the exponent $-14/5$ follows from $-y - 2|y'|$. We note that the potential exponents $-y - 1$ and $-2y$ do not appear in (41).

The analysis leading to (39) and (41) and the relation with conformal field theory is given in appendix F.

5.1.4. Comparison with the equimodular curve of $\kappa_\pm(z)$

In figure 9 we compare the zeros for the 39×39 lattice with the equimodular curve of the $\kappa_\pm(z)$ of figure 2. Unlike the comparisons of figure 4 the $\kappa_\pm(z)$ equimodular
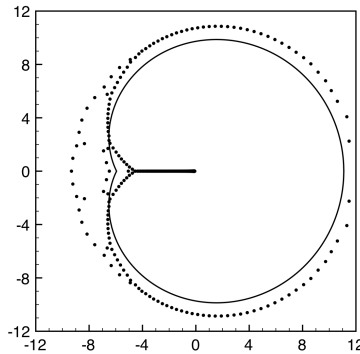
Figure 9. The equimodular curves for $|\kappa_-(z)| = |\kappa_+(z)|$ in the complex z plane and the partition function zeros for cylindrical boundary conditions on the 39×39 lattice

curve does not have a region of overlap with the zeros of the 39×39 lattice. However, in the region to the right of the necklace, if

$$\lim_{L_h \to \infty, L_v \to \infty} Z_{L_v, L_h}(z)^{1/L_v L_h} \qquad \text{is independent of} \quad L_v/L_h,$$

then, for this region, the limiting locus of zeros will agree with the $\kappa_\pm$ equimodular curve. We have examined this possibility and find that we can well fit this portion of the zero locations of figure 7 by a shifted cardioid

$$\text{Re}(z) = \frac{a}{2} + c + a \cos\theta + \frac{a}{2} \cdot \cos 2\theta,$$
$$\text{Im}(z) = a \sin\theta + \frac{a}{2} \cdot \sin 2\theta. \tag{43}$$

The fitting parameters a and c depend on L, and, when plotted versus $1/L$, these values fall very closely on a straight line which extrapolated to $L \to \infty$ gives a curve which is virtually indistinguishable from the $\kappa_\pm$ equimodular curve outside of the necklace regions. We take this to be evidence that in this non necklace region the limit (43) for cylindrical boundary conditions is independent of the ratio L_v/L_h. Further numerical details are given in Appendix D.

5.2. Toroidal boundary conditions

It is numerically more difficult to compute partition function zeros for toroidal boundary conditions and the maximum size we have been able to study is 27×27. These results are plotted in figure 10. There is a necklace for $L \geq 12$ and there are zeros in the necklace region for 15×15 through 21×21. For 24×24 and 27×27 there are no zeros in the necklace region.
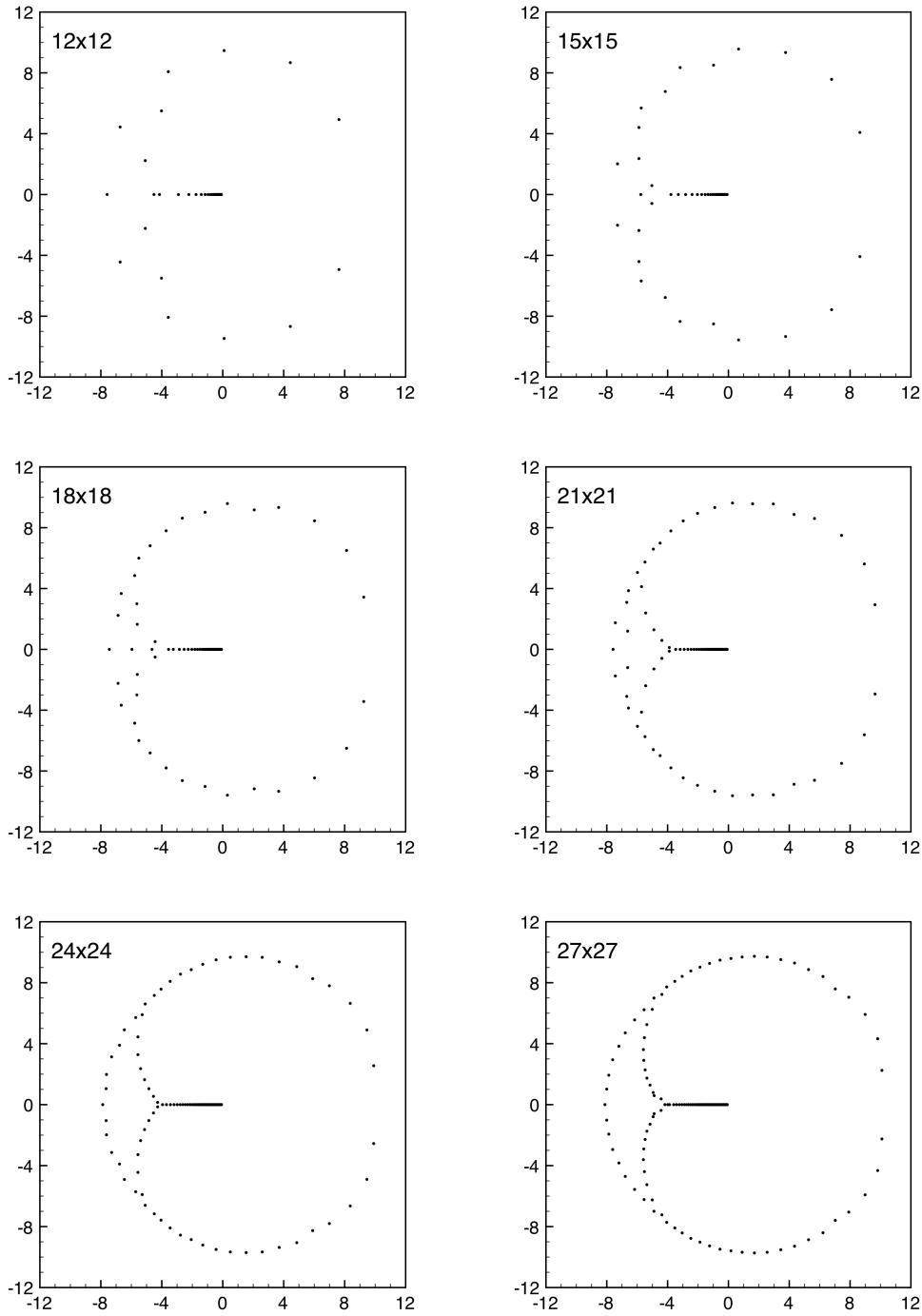
Figure 10. Plots of partition function zeros in the complex fugacity plane z for hard hexagon with toroidal boundary conditions of size $L \times L$ with $L = 12, 15, 18, 21, 24, 27$. The value of $L \times L$ is given in the upper left hand corner of the plots.

5.2.1. Comparison with the equimodular curve of $\kappa_{\pm}(z)$

In figure 11 we compare the partition function zeros for toroidal boundary conditions on the 27×27 lattice with the equimodular curve of $\kappa_{\pm}(z)$. Outside of the necklace region the agreement is much closer than it was for the cylindrical case for the 39×39 lattice. It is appealing to attribute this agreement with the absence of boundary effects.
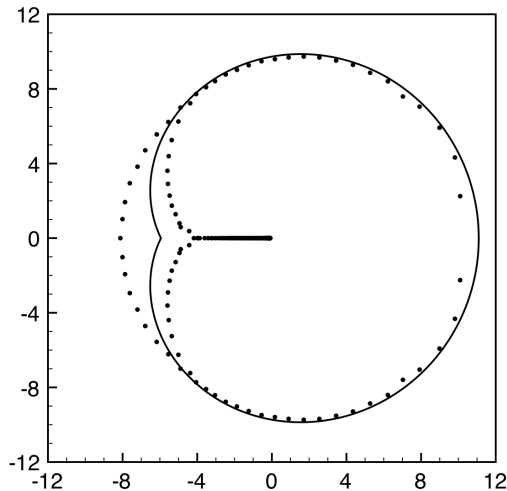
Figure 11. The equimodular curves for $|\kappa_{-}(z)| = |\kappa_{+}(z)|$ in the complex z plane and the partition function zeros for toroidal boundary conditions on the 27×27 lattice

5.2.2. Dependence on the aspect ratio L_v/L_h

We conclude our study of partition function zeros by examining the dependence of the zeros on the aspect ratio L_v/L_h of the $L_h \times L_v$ lattices. In figure 12 we plot the partition function zeros for the toroidal lattices of various ratios L_v/L_h as large as 40 for $L_h = 15, 18, 21$. We see that the number of zeros outside the main curve increases for fixed L_h with increasing aspect ratio and for fixed aspect ratio decreases with increasing L_h. It is furthermore obvious that even for an aspect ratio of 40 there are remarkably few zeros on the rays seen in the transfer matrix equimodular curves of figure 5. From this we conclude, for fixed $L_v/L_h < \infty$ with $L_h \to \infty$, that the partition function zeros of the $L_h \times L_v$ on the toroidal lattice will not have any rays of zeros which extend to infinity.
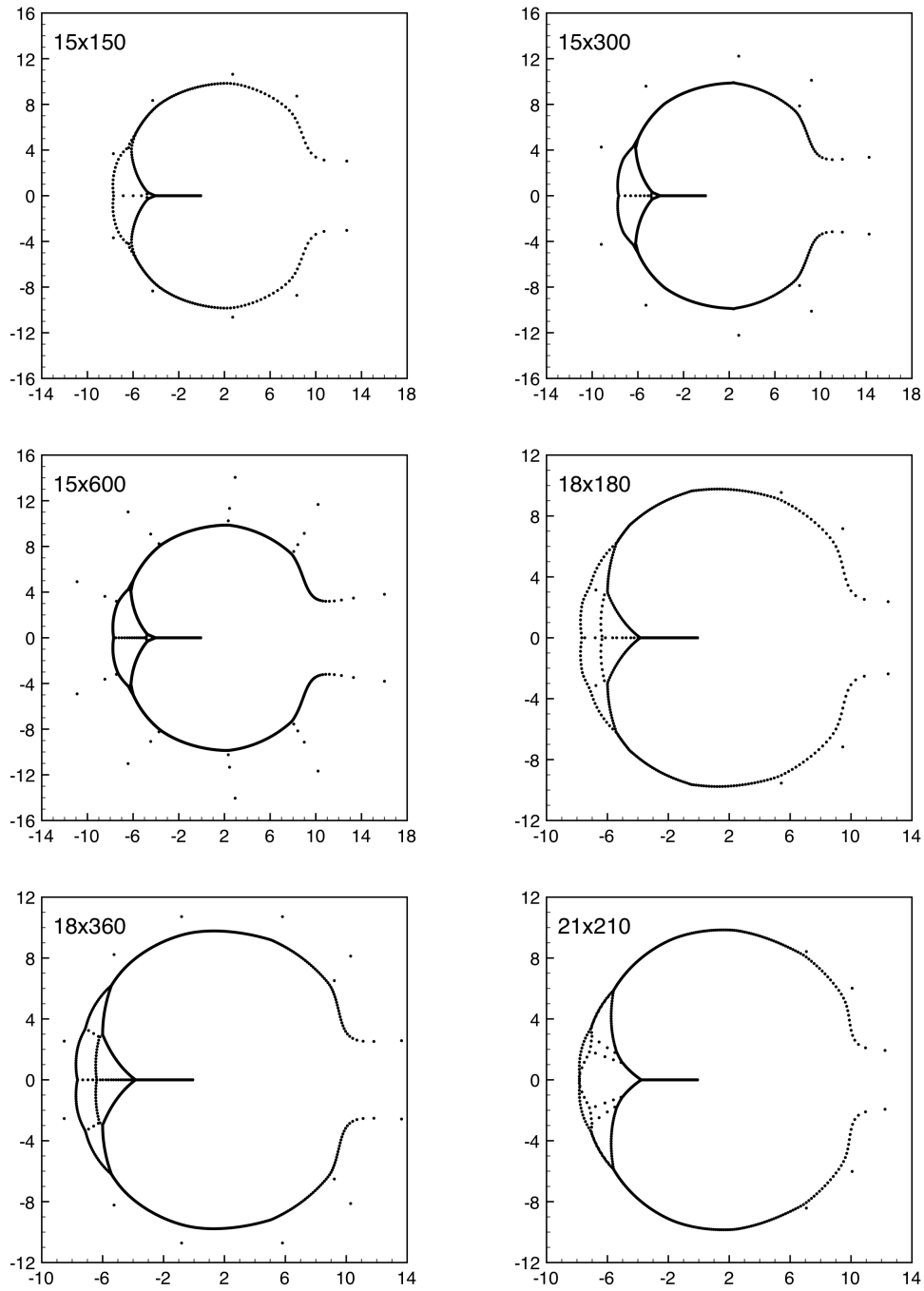
Figure 12. Partition function zeros for toroidal boundary conditions on the lattices 15 × 150, 15 × 300, 15 × 600, the lattices 18 × 180, 18 × 360 and the lattice 21 × 210. The number of points off of the main curve for fixed aspect ratio L_v/L_h decreases with increasing L_h.

5.3. Density of zeros for $z_y \leq z \leq z_d$

On the negative z axis we label as z_j the position of the jth zero where z_1 is the zero nearest to $z = 0$ and z_y is the zero closest to the Y branching on the negative z axis. Then calling N_L the number of zeros in the interval $z_y \leq z \leq 0$ on a finite lattice of size $L \times L$ the density $D(z)$ in the thermodynamic limit is proportional to

$$D(z) = \lim_{L \to \infty} D_L(z_j) \qquad \text{where} \qquad D_L(z_j) = \frac{1}{N_L \cdot (z_j - z_{j+1})}. \tag{44}$$

This density of zeros will diverge at z_d as $(1 - z/z_d)^{-1/6}$, which is obtained from the leading term in the expansion of $\rho_-(z)$. This expansion is obtained, in Appendix B, from the algebraic equation (see eqn. (12.10) in [5]) as

$$\rho_-(z) = t_d^{-1/6} \cdot \Sigma_0(t_d) + \Sigma_1(t_d) + t_d^{2/3} \cdot \Sigma_2(t_d) + t_d^{3/2} \cdot \Sigma_3(t_d)$$
$$+ t_d^{7/3} \cdot \Sigma_4(t_d) + t_d^{19/6} \cdot \Sigma_5(t_d), \tag{45}$$

where $t_d = 5^{-3/2} \cdot (1 - z/z_d)$, the fractional powers are all defined positive for positive t_d and where the $\Sigma_i(t_d)$ read

$$\Sigma_0 = -\frac{1}{\sqrt{5}} + \frac{1}{12}\left(5 + \frac{11}{\sqrt{5}}\right)t_d + \frac{1}{144}\left(275 + \frac{639}{\sqrt{5}}\right)t_d^2 + \frac{1}{1296}\left(17765 + \frac{37312}{\sqrt{5}}\right)t_d^3 + \cdots$$

$$\Sigma_1 = \frac{1}{2}\left(1 + \frac{1}{\sqrt{5}}\right) + \frac{1}{\sqrt{5}}t_d + \frac{1}{2}\left(5 - \frac{1}{\sqrt{5}}\right)t_d^2 - \frac{1}{2}\left(5 - \frac{83}{\sqrt{5}}\right)t_d^3 + \cdots$$

$$\Sigma_2 = -\frac{2}{\sqrt{5}} - \frac{2}{15}(25 - 4\sqrt{5})t_d + \frac{4}{45}(125 - 108\sqrt{5})t_d^2 - \frac{4}{405}(16775 - 4621\sqrt{5})t_d^3 + \cdots$$

$$\Sigma_3 = -\frac{3}{\sqrt{5}} - \frac{3}{4}\left(15 - \frac{7}{\sqrt{5}}\right)t_d + \frac{3}{16}\left(175 - \frac{1189}{\sqrt{5}}\right)t_d^2 - \frac{21}{16}\left(705 - \frac{646}{\sqrt{5}}\right)t_d^3 + \cdots$$

$$\Sigma_4 = -\frac{4}{\sqrt{5}} - \frac{2}{15}(175 - 13\sqrt{5})t_d + \frac{2}{45}(1625 - 2637\sqrt{5})t_d^2 - \frac{52}{405}(22100 - 3499\sqrt{5})t_d^3 + \cdots$$

$$\Sigma_5 = -\frac{6}{\sqrt{5}} - \frac{1}{2}\left(95 - \frac{31}{\sqrt{5}}\right)t_d + \frac{1}{24}\left(3875 - \frac{34641}{\sqrt{5}}\right)t_d^2 - \frac{31}{216}\left(55685 - \frac{40892}{\sqrt{5}}\right)t_d^3 + \cdots$$
$$\tag{46}$$

The term in $t_d^{2/3}$ was first obtained by Dhar [18] but the full expansion has not been previously reported. The form (45) follows from the renormalization group expansion [16] of the singular part of the free energy at $z = z_d$

$$f_s = t_d^{2/y} \cdot \sum_{n=0}^{4} t_d^{-n(y'/y)} \cdot \sum_{m=0}^{\infty} a_{n;m} \cdot t_d^m, \tag{47}$$

where $y = 12/5$ is the leading renormalization group exponent for the Yang-Lee edge, and $y' = -2$, the exponent for the contributing irrelevant operator which breaks rotational invariance on the triangular lattice, is determined from the term $t_d^{2/3}$ in (45).

The density $\rho_-(z)$ has singularities only at z_d and z_c in the plane cut on $\infty \leq z \leq z_d$ and $z_c \leq z \leq \infty$. However, this does not require that the series (46) for $\Sigma_j(t_d)$ will have t_d evaluated at z_c as their radii of convergence. We have investigated this by computing the coefficients $c_j(n)$ of z^n in the series for $\Sigma_j(t_d)$ using Maple up to $n = 1200$. For $\Sigma_0(t_d)$ these coefficients are all positive for $n > 1$ and for $\Sigma_j(t_d)$ with $j = 2, 3, 4$ all coefficients are negative. However, for $\Sigma_5(t_d)$ the coefficients are negative

for $0 \leq n \leq 19$ and positive for $n \geq 20$. For $\Sigma_1(t_d)$ the coefficients are positive for $0 \leq n \leq 554$ and negative for $n \geq 555$. Furthermore the ratios $r_j = c_j(n)/c_j(n+1)$ seem to be converging to $2^{-3/2} = 0.08944271 \cdots$ which corresponds to $z = 0$.

We investigate the density $\rho_-(z)$ further by plotting, in figure 13, $D_L(z_j)$ as a function of z computed from the zeros of the $L \times L$ lattice with cylindrical boundary conditions for $L = 33, 36, 39$. The values of $D_L(z_j)$ for all three lattices lie remarkably close to the same curve except for the region $-0.093 < z < z_d$, where some scatter is observed which is caused by the finite size of the lattice.
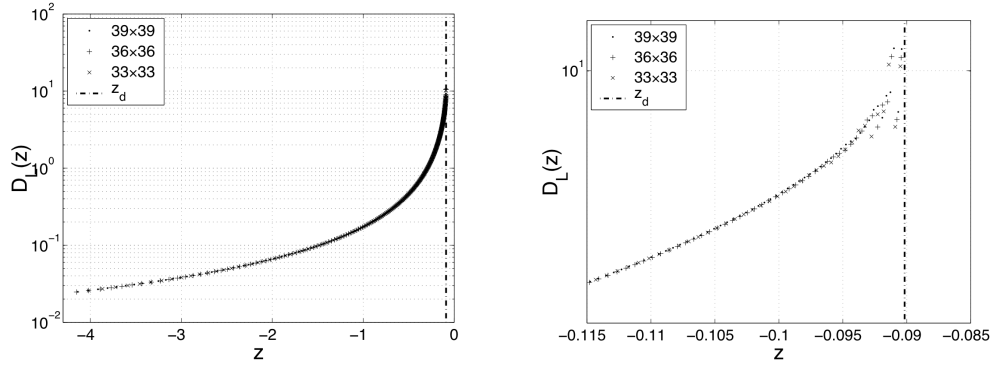
Figure 13. Log plots of the density of zeros $D_L(z_j)$ on the negative z axis for $L \times L$ lattices with cylindrical boundary conditions. The figure on the right is an expanded scale near the singular point z_d.
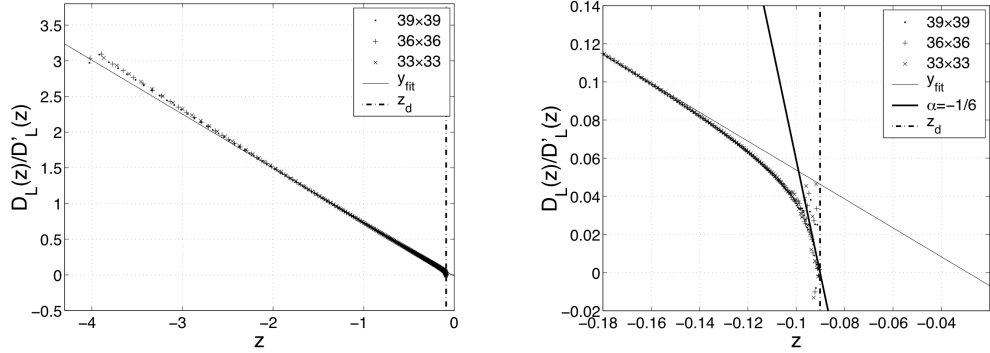
Figure 14. Plots of $D_L(z_j)/D'_L(z_j)$ on the negative z axis for $L \times L$ lattices with cylindrical boundary conditions. For the plot on the left it is impressive that for the range $-4.0 \leq z \leq -0.14$ the data is extremely well fitted by the power law form (48) with an exponent -1.32 (which corresponds to a slope of -0.76) and an intercept $z_f = -0.029$. The plot on the right is an expanded scale near z_d and the line passing through $z = z_d$ with slope of -6 is plotted for comparison which corresponds to the true exponent $= -1/6$ which only is observed in a very narrow range near z_d of $-0.095 \leq z \leq z_d = -0.0901 \cdots$.

To estimate the divergence of $D(z)$, at $z = z_d$, we write for z near z_d

$$D(z) \sim A \cdot (z_d - z)^\alpha \quad \text{and thus} \quad \frac{D(z)}{D'(z)} \sim \frac{z_d - z}{\alpha}, \tag{48}$$

where $D'(z)$ is the derivative of $D(z)$. In figure 14 we plot $D_L(z_j)/D'_L(z_j)$, where we define

$$D'_L(z_j) = \frac{D_L(z_{j+1}) - D_L(z_j)}{z_{j+1} - z_j}. \tag{49}$$

For z, away from z_d, the plot is very well fitted by the z-line

$$\frac{D_L(z)}{D'_L(z)} \sim \frac{z_f - z}{\alpha}, \tag{50}$$

with $\alpha_f = -1.32 \cdots$ (or $\alpha_f^{-1} = -0.76 \cdots$), and $z_f = -0.029 \cdots$ However, for $-0.14 \leq z \leq z_d$ this fit is no longer valid. We make in figure 14 a comparison with the true value of $\alpha = -1/6$, which is obtained from $\kappa_-(z)$. This figure vividly illustrates the very limited range of validity for the use of perturbed conformal field theory and scaling arguments to describe systems away from critical points. The same phenomenon has been seen in [19, eqn. (4.8) and Fig. 4] for Hamiltonian chains.

6. Discussions

The results of the numerical studies presented above allow us to discuss in some detail the relation of the functions $\kappa_\pm(z)$, which completely describe the hard hexagon partition function per site on the positive z axis, with the partition function per site in the full complex z plane. In particular the approach to the thermodynamic limit, the existence of the necklace, the relation to the renormalization group and questions of analyticity will be addressed.

6.1. The thermodynamic limit

When the fugacity z is real and positive the free energy and the partition function per site is independent of the aspect ratio L_v/L_h of the $L_h \times L_v$ lattice as $L_h, L_v \to \infty$, and will be the same for both cylindrical and toroidal boundary conditions. This is a necessary condition for thermodynamics to be valid.

However, the example of hard squares at $z = -1$, where it is found [6]-[9] that the partition function $Z_{L_v, L_h}(-1)$ depends on number theoretic properties of L_v and L_h, demonstrates that there may be places in the complex z plane where a thermodynamic limit independent of L_v/L_h does not exist. We have investigated in sections 4 and 5 the extent to which our data supports the conclusion that for complex z there is a thermodynamic limit independent of the aspect ratio L_v/L_h as stated in (19). If this independence holds then the limiting locus of partition function zeros will lie on the limiting locus of transfer matrix equimodular curves. However, the converse does not need to be true and there is no guarantee that zeros will lie on all limiting loci of transfer matrix eigenvalues. In particular we have argued in sections 4.3 and 5.2.2 that for toroidal boundary conditions there will be no zeros in the rays which go to infinity.

6.2. Existence of the necklace

All the data both for partition function zeros and transfer matrix eigenvalues contain a necklace in the left half plane. Such a necklace is incompatible with a partition function which only includes the functions $\kappa_{\pm}(z)$.

For cylindrical boundary conditions it is clear from figures 3 and 4 that the limiting locus of transfer matrix equimodular curves in the necklace region has not yet been obtained. Furthermore in figures 3 and 4 there are equimodular curves inside the necklace region beginning at $L_h = 18$ whereas in figure 7 partition function zeros only appear clearly inside the necklace region for lattices 30×30 and greater.

For toroidal boundary conditions the dominance of the $P = 0$ sector in the limit $L_h \to \infty$, discussed in section 4.3.2, implies that in the thermodynamic limit the necklace will be the same as for cylindrical boundary conditions.

The simplest mechanism which will account for this behavior is for there to be one (or more) extra eigenvalue(s) of the transfer matrix which becomes dominant in the necklace region. Further analytic computation is needed to verify this mechanism. However, the present data does not rule out the possibility that for sufficiently large systems the necklace region could be filled with zeros.

6.3. Relation to the renormalization group

The form of the singularity of the density $\rho_{-}(z)$ at $z = z_d$ given in section 5.3 in (47) is not the most general form, allowed by the renormalization group. The most general form allows the singular part of the free energy to have $y' = -1$, which would give a term in (45) with exponent $t_d^{1/4}$ (which is, in fact, not present). This may be explained by the following renormalization group argument given by Cardy [20]. The integer corrections given by ny' are conformal descendants of the identity operator. The total scaling dimension of these operators is $N + \bar{N}$. Their conformal spin is $N - \bar{N}$, where N and $\bar{N}$ are nonnegative integers, and the corresponding exponent y' is $2 - N - \bar{N}$. However, the six fold lattice symmetry of the hard hexagon model allows only operators with $N - \bar{N} \equiv 0 \pmod 6$. Therefore the dimensions y' cannot be odd which is what is observed in (45). The same conclusion will apply also to hard squares but not for hard triangles.

6.4. Analyticity of the partition function

The final property to be discussed is the relation of the analyticity of the free energy obtained by analytically continuing the free energy from the positive z axis into the complex z plane.

For hard hexagons the functions $\kappa_{\pm}(z)$ have singularities only at $z = z_d, z_c, \infty$, whereas the partition function per site in the complex plane fails to be analytic at those boundaries which are the thermodynamic limit of the equimodular curves. It is obvious for hard hexagons that these boundaries have nothing to do with the analyticity of $\kappa_{\pm}(z)$. However it is unknown if in general the partition function per site on the real axis can be continued analytically beyond the region where it corresponds to the maximum modulus of the transfer matrix eigenvalue.

The other locus where the hard hexagon model has partition function zeros is on the negative real axis for $z \leq z_d$. These zeros correspond to the complex conjugate solutions for $\kappa_{-}(z)$ alone and have no connection with $\kappa_{+}(z)$. The leading singular behavior of hard hexagons at z_d is believed to be a property shared by all systems

with purely repulsive (positive) potentials and is a universal repulsive-core singularity [21, 22]. Therefore it is of considerable interest to determine whether the ability to continue through this locus of zeros, which is the case for the integrable system of hard hexagons, will hold for all the non-integrable models in the same universality class.

7. Conclusion

The hard hexagon model solved by Baxter [1, 2] not only satisfies the Yang-Baxter equation but also as shown by Joyce [5] and Tracy *et al* [28, 29] has a remarkable structure in terms of algebraic modular functions and their associated Hauptmoduls. It is thus a good candidate for a global analysis in the whole complex plane of the partition function per site which is complementary to a local analysis based on series expansions and perturbation theory.

In this paper we have made a precision finite size study for the hard hexagon model of the zeros of the partition function and of the equimodular curves of the transfer matrix in the complex fugacity plane z. This study reveals that the partition function per site has more structure for complex z than has been seen in previous studies on much smaller systems [24]-[27]. In particular our results demonstrate that the conjecture on zeros of the hard hexagon partition function made in [27] is incorrect, and corresponds to a too simple high density equimodular condition of the Hauptmodul being real. This condition has to be replaced by more involved equimodular conditions involving both the low and high density partition functions. Furthermore we have found that the results of [1, 2] on the positive z axis are not sufficient to determine all of the analytic structure of the partition function per site in the complex z plane.

The full significance of our results is to be seen in the comparison with hard squares and with the Ising model in a magnetic field which do not satisfy a Yang-Baxter equation and will not have the global properties of modular functions. In particular we note that in section 4.1.2 it was found that on the negative z axis the zeros of the resultant of the characteristic equation of the transfer matrix have the remarkable property that their multiplicity is two. This is in distinct contrast with hard squares where the multiplicity of the roots of the resultant is one.

Hard squares and hexagons are the limiting case of Ising models in a magnetic field when the field becomes infinite. The results of this paper have extensions to Ising models in a finite magnetic field which will be presented elsewhere.

Appendix A. The singularities of $\kappa_\pm(z)$

The partition functions per site $\kappa_\pm(z)$ are singular at z_c, z_d and ∞. At $z = z_c$, and $z = z_d$, the values of the three Ω_i read respectively

$$\Omega_1(z_c) = 0, \qquad \Omega_2(z_c) = (5^{5/2}z_c)^2, \qquad \Omega_3(z_c) = -(5^{5/2}z_c)^3, \tag{A.1}$$

$$\Omega_1(z_d) = 0, \qquad \Omega_2(z_d) = (5^{5/2}z_d)^2, \qquad \Omega_3(z_d) = (5^{5/2}z_d)^3. \tag{A.2}$$

Appendix A.1. High density

As $z \to \infty$ the physical $\kappa_+(z)$, which satisfies the algebraic equation (33), diverges. There is only one such real solution and by direct expansion of (33) we find that

$$\kappa_+(z) = z^{1/3} + \frac{1}{3}z^{-2/3} + \frac{5}{9}z^{-5/3} + \frac{158}{81}z^{-8/3} + \frac{2348}{243}z^{-11/3} + \cdots \tag{A.3}$$

which agrees with eqn. (7.14) in [5]. It follows from (A.3) that $\kappa_+(z)$ has a branch cut on the segment $-\infty < z \le z_d$ and that on this segment the phase is

$$e^{\pm\pi i/3} \qquad \text{for} \qquad \mathrm{Im}\, z = \pm\epsilon \to 0. \tag{A.4}$$

When $z_c < z < \infty$ there is one real positive, one real negative, and one complex conjugate pair of solutions to the fourth order equation (33) for κ_+^6. The negative solution is larger in magnitude than the positive solution, and, thus, cannot correspond to any eigenvalue of the transfer matrix. However, the magnitude of the complex conjugate pair of solutions is less than the value of the real positive root. At $z = z_c$ the real positive root collides with the complex conjugate pair.

When $z = z_c$, introducing the rescaled variable

$$w_{c+} = \Omega_3(z_c) \cdot \frac{\kappa_+^6(z_c)}{z_c^6} = -(5^{5/2}/z_c)^3 \cdot \kappa_+^6(z_c), \tag{A.5}$$

we find that (33) reads $(w_{c+} + 3^9)^3 = 0$. Thus, using (A.5) and the fact that $\kappa_+(z_c)$ must be positive, we obtain

$$\kappa_+(z_c) = (3^3 \cdot 5^{-5/2} z_c)^{1/2} = 2.3144003 \cdots \tag{A.6}$$

which is (7.17) of [5].

For $z = z_d$, introducing the rescaled variable $w_{d+} = \Omega_3(z_d) \cdot \kappa_+^6(z_d)/z_d^6 = (5^{5/2}/z_d)^3 \cdot \kappa_+^6(z_d)$, we find that (33) also reads $(w_{d+} + 3^9)^3 = 0$. Using (A.4), one gets $\kappa_+(z_d)^6 = 3^9/5^8 (1525 - 682\, 5^{1/2})$ or $\kappa_+(z_d) = e^{\pm\pi i/3}\, 0.208689 \cdots$.

Appendix A.2. Low density

When $z = z_c$ equation (35) reduces using (A.1) to the eleventh order equation

$$f_-(z_c, w_{c-}) = \sum_{k=0}^{11} \tilde{C}_k^- \cdot w_{c-}^k = 0 \tag{A.7}$$

with $w_{c-} = 5^{5/2}\kappa_-^2(z_c)/z_c$ and

$$\tilde{C}_0^- = -2^{32} \cdot 3^{27},$$
$$\tilde{C}_1^- = 0,$$
$$\tilde{C}_2^- = 2^{26} \cdot 3^{23} \cdot 31,$$
$$\tilde{C}_3^- = -2^{26} \cdot 3^{19} \cdot 47,$$

$$\tilde{C}_4^- = -2^{17} \cdot 3^{18} \cdot 5701,$$
$$\tilde{C}_5^- = 2^{16} \cdot 3^{14} \cdot 7^2 \cdot 19 \cdot 37,$$
$$\tilde{C}_6^- = -2^{10} \cdot 3^{10} \cdot 7 \cdot 273001,$$
$$\tilde{C}_7^- = 2^9 \cdot 3^{10} \cdot 11 \cdot 13 \cdot 139,$$
$$\tilde{C}_8^- = -3^5 \cdot 7 \cdot 1028327,$$
$$\tilde{C}_9^- = 37 \cdot 79087,$$
$$\tilde{C}_{10}^- = -19 \cdot 139,$$
$$\tilde{C}_{11}^- = 1, \tag{A.8}$$

which factorizes as

$$f_-(z_c, w_{c-}) = (w_{c-} + 2^4)^2 \cdot (w_{c-} - 3^3)^3 \cdot (w_{c-} - 2^4 \cdot 3^3)^6 = 0. \tag{A.9}$$

From the second factor in (A.9) we obtain the solution

$$\kappa_-(z_c) = (3^3 \cdot 5^{-5/2} z_c)^{1/2} = \kappa_+(z_c), \tag{A.10}$$

as required by continuity. At $z = z_c$ the solution for $\kappa_-(z_c)$ is three fold degenerate which also agrees with the degeneracy of $\kappa_+(z_c)$.

For $0 < z < z_c$ there is one real positive, one real negative and five complex conjugate solutions of the 12th order equation (35). Three of the complex conjugate pairs have a modulus less than the real positive solution. At $z = z_c$ a collision of the real positive root with one of the complex conjugate pairs occurs.

When $z = z_d$ an analogous reduction can be made by use of (A.2) and of the rescaling $w_{d-} = 5^{5/2} \kappa_-^2(z_d)/z_d$. We find, in analogy to (A.9), the factorization

$$f_-(z_d, w_{d-}) = -(w_{d-} - 2^4)^2 \cdot (w_{d-} + 3^3)^3 \cdot (w_{d-} + 2^4 \cdot 3^3)^6 = 0. \tag{A.11}$$

At $z = z_d$ the last factor in (A.11) vanishes and we find

$$\kappa_-(z_d) = (-2^4 \cdot 3^3 \cdot 5^{-5/2} z_d)^{1/2} = (2^4 \cdot 3^3 \cdot 5^{-5/2}/z_c)^{1/2}$$
$$= 4 |\kappa_+(z_d)| = 0.83475738 \cdots. \tag{A.12}$$

For $z_d < z < 0$ there are three real positive, three real negative, and three complex conjugate solutions of the polynomial relation (35) of degree twelve in κ_-^2, and all three of the complex conjugate solutions have a modulus smaller than the largest positive real solution. The largest positive real solution is the dominant eigenvalue, until $z = z_d$, when a collision with the next real largest solution and two complex conjugate pairs occurs.

Appendix B. Expansion of $\rho_-(z)$ at z_c and z_d

The low density function $\rho_-(z)$ satisfies the polynomial equation of degree twelve in ρ_- and degree four in z (see eqn. (12.10) in [5])

$$\rho_-^{11} \cdot (\rho_- - 1) \cdot z^4 \quad - [\rho_-^5 z^3 - (\rho_- - 1)^5 z] \cdot p_7$$
$$+ \rho_-^2 \cdot (\rho_- - 1)^2 \cdot p_8 \cdot z^2 \quad + \rho_- \cdot (\rho_- - 1)^{11} = 0 \tag{B.1}$$

where

$$p_7 = 22\rho_-^7 - 77\rho_-^6 + 165\rho_-^5 - 220\rho_-^4 + 165\rho_-^3 - 66\rho_-^2 + 13\rho_- - 1,$$
$$p_8 = 119\rho_-^8 - 476\rho_-^7 + 689\rho_-^6 - 401\rho_-^5 - 6\rho_-^4 + 125\rho_-^3 - 63\rho_-^2 + 13\rho_- \tag{B.2}$$

This equation has the remarkable property that at $z = z_c$, z_d it reduces to a fifth order equation

$$-\frac{275 + 123\sqrt{5}}{8000} \cdot (10\rho_- - 5 + \sqrt{5})^5 = 0 \qquad \text{for} \quad z = z_c, \tag{B.3}$$

$$-\frac{275 - 123\sqrt{5}}{8000} \cdot (10\rho_- - 5 - \sqrt{5})^5 = 0 \qquad \text{for} \quad z = z_d. \tag{B.4}$$

There are four distinct Puiseux expansions of ρ_- about z_c which are real for $z < z_c$. The leading exponents of these expansions are -1, $-1/6$, 0, 0. The physical solution must be finite at $z = z_c$ and we see from (B.3) that the two solutions which are constant at $z = z_c$ have the value $\rho_-(z_c) = (1 - 5^{-1/2})/2$. To decide which of these two Puiseux expansions is the correct physical solution we need the independent condition that the leading nonanalytic term has exponent $2/3$. The result [5, 12.15] follows from this additional condition.

At $z = z_d$ there are also four Puiseux expansions of $\rho_-(z)$ which are real for $z_d < z$. The leading exponents are, again, -1, $-1/6$, 0, 0. Now, unlike $\rho_-(z_c)$, the density is not constant at $z = z_d$, but diverges with exponent $-1/6$. Furthermore, in the cluster expansion of $\rho_-(z)$ about $z = 0$, it follows, from a theorem of Groeneveld [23], that because the sign of the coefficient of z^n is $(-1)^{n-1}$, the density must be negative in the segment $z_d < z < 0$. The leading term of the Puiseux expansion with exponent -1 is positive and is, thus, excluded. There are six conjugate solutions with exponent $-1/6$. The member of this class which has the correct negative behavior $z \to z_d+$ is the result given in (45).

Appendix C. The Hauptmodul equations and the $\kappa_\pm$ equimodular curves

The equations (33) and (35) for $\kappa_\pm$ may be usefully re-expressed in terms of the Hauptmodul H

$$H = 1728\, z \cdot \frac{\Omega_1^5(z)}{\Omega_3^2(z)}, \tag{C.1}$$

by making the rescaling

$$W_\pm = \Omega_3(z) \cdot \left(\frac{\kappa_\pm}{z}\right)^6. \tag{C.2}$$

For high density it is straight forward to use (C.1) and (C.2) in (33) to obtain

$$\begin{aligned} P_+(W_+, H) &= H^2 \cdot W_+^4 + 2^7 \cdot 3^6 \cdot (27\,H - 32) \cdot W_+^3 \\ &+ 2^7 \cdot 3^{16} \cdot (45\,H - 32) \cdot W_+^2 - 2^{12} \cdot 3^{25}\, W_+ - 2^{12} \cdot 3^{33} = 0. \end{aligned} \tag{C.3}$$

The algebraic curve $P_+(W_+, H) = 0$ is the union of two genus zero curves.

For low density the polynomial relation (35) on κ_- in the z variable can be written in terms of the Hauptmodul (C.1), and of the rescaled variable W_- (C.2), as follows

$$\begin{aligned} P_-(W_-, H) &= H^6 \cdot W_-^{12} + 2^{12} \cdot 3^7 \cdot P_{11} \cdot W_-^{11} + 2^{19} \cdot 3^{13} \cdot P_{10} \cdot W_-^{10} \\ &- 2^{32} \cdot 3^{18} \cdot P_9 \cdot W_-^9 - 2^{36} \cdot 3^{29} \cdot P_8 \cdot W_-^8 + 2^{52} \cdot 3^{38} \cdot P_7 \cdot W_-^7 \\ &+ 2^{62} \cdot 3^{46} \cdot P_6 \cdot W_-^6 - 2^{77} \cdot 3^{56} \cdot P_5 \cdot W_-^5 - 2^{85} \cdot 3^{65} \cdot P_4 \cdot W_-^4 \\ &+ 2^{100} \cdot 3^{73} \cdot P_3 \cdot W_-^3 - 2^{110} \cdot 3^{83} \cdot P_2 \cdot W_-^2 + 47 \cdot 2^{126} \cdot 3^{92} \cdot W_- \\ &- 2^{132} \cdot 3^{99} = 0, \end{aligned} \tag{C.4}$$

where the polynomials P_n read:

$$
\begin{aligned}
P_{11} = {}& 85423588659\,H^5 - 1273194070087\,H^4 + 5683675368960\,H^3 \\
& - 3624245 \cdot 2^{12} \cdot 3^6\,H^2 + 901 \cdot 2^{19} \cdot 3^9\,H - 2^{24} \cdot 3^{11}, \\
P_{10} = {}& 2098366262345322754767\,H^5 - 4991131592299977169590\,H^4 \\
& + 3893219286516719759223\,H^3 - 1056221406812154079936\,H^2 \\
& + 56427952366139092992\,H - 483780265 \cdot 2^{17} \cdot 3^5, \\
P_9 = {}& 1538272325441267387131 8753\,H^4 + 26277083153777345473689849\,H^3 \\
& + 40984221205680476559 74595\,H^2 + 3792122970706028673 7587\,H \\
& + 1560354561975860656, \\
P_8 = {}& 102093912526673507175090 4401\,H^4 - 1161800973997140083525143956\,H^3 \\
& + 21439380149031311272647 0774\,H^2 - 20060704883387984152 38516\,H \\
& + 591909552463296489 61, \\
P_7 = {}& 5086974009978429599163 51\,H^3 - 554351605658908065490725\,H^2 \\
& - 351928009763942038320 51\,H - 2775596721861024679, \\
P_6 = {}& 1245962466251450908065\,H^3 - 1525544981578249672 8645\,H^2 \\
& + 8457596543456744207175\,H - 13332664262978720611, \\
P_5 = {}& 114630292396020573\,H^2 - 366034684810378734\,H + 92792159042784817, \\
P_4 = {}& 938107512437391\,H^2 - 1026461977730478\,H + 933965999427127, \\
P_3 = {}& 121395557277\,H - 59327302513, \\
P_2 = {}& 11532609\,H - 1281659. \tag{C.5}
\end{aligned}
$$

Do note that the algebraic curve $P_-(W_-, H) = 0$ is actually a genus zero curve. The algebraic curve (C.4) is the sum of 43 monomials of degree six in H and degree 12 in W_-, as compared to a sum of 157 monomials of degree 22 in z and degree 24 in κ_- for (35). At first sight, the polynomial relation (C.4), in the Hauptmodul and the rescaled variable W_-, looks quite different from (35). In fact, the two polynomial relations (C.4) and (35) are in agreement, as can be seen on the quite remarkable identity

$$
z^{66} \cdot P_-(W_-, H) = 12^{18} \cdot f_-(z, \kappa_-) \cdot f_-(z, e^{2\pi i/3}\,\kappa_-) \cdot f_-(z, e^{-2\pi i/3}\,\kappa_-), \tag{C.6}
$$

where the l.h.s. of (C.6) is actually a polynomial expression in terms of κ_- and z.

Appendix C.1. $\quad \kappa_+$ *versus* κ_-

The functions κ_- and κ_- are not related by analytic continuation. However, because both W_+ and W_- are algebraic functions of the same Hauptmodul we can eliminate H between (C.3) and (C.4) to obtain the following algebraic relation between W_+ and W_-

$$
\begin{aligned}
& {W_-}^4\,{W_+}^6 + 32\,{W_-}^3\,W_+^5 \cdot (1509\,W_- - 512\,W_+) \\
& - 2\,W_-^2\,W_+^3 \cdot (W_-^3 - 411832512\,W_-^2\,W_+ + 937623552\,W_-\,W_+^2 - 50331648\,W_+^3) \\
& - 32\,W_-\,W_+^2 \cdot (34791\,W_-^4 - 182579836224\,W_-^3 W_+ - 1128985165824\,W_-^2\,W_+^2 \\
& \qquad - 549067948032\,W_-\,W_+^3 + 8589934592\,W_+^4) \\
& + (W_-^4 - 84091500544\,W_-^3\,W_+ - 1482164797440\,W_-^2\,W_+^2 - 8145942347776\,W_-\,W_+^3 \\
& \qquad + 68719476736\,W_+^4) \cdot (W_-^2 - 172928\,W_-\,W_+ + 4096\,W_+^2) = 0. \tag{C.7}
\end{aligned}
$$

This remarkable algebraic relation for hard hexagons follows from the modular properties of κ_+ and κ_- and is not expected to exist for a generic system.

One verifies easily that eliminating W_+ between (C.3) and (C.7) one recovers (C.4), and that eliminating W_- between (C.4) and (C.7) one recovers (C.3).

The polynomial relation (C.7) of degree six in W_+ and W_-, is actually also a genus zero algebraic curve.

The situations where $\kappa_- = \kappa_+$ (see (A.10)) correspond to $W_- = W_+$ in (C.7). It yields the values $0, -3^9, -57707, 22743 \pm 30268\,i$, corresponding to $W_- = W_+ = -3^9$. Note that $\kappa_- = .83475738\cdots$ in (A.12) corresponds to the integer value $W_- = -2^{12}\,3^9$.

Appendix C.2. The $\kappa_\pm$ equimodular curves

The $\kappa_\pm$ equimodular condition reads $|W_+| = |W_-|$ in terms of $W_\pm$. Setting the ratio

$$r = \frac{W_+}{W_-}, \tag{C.8}$$

we can obtain a polynomial relation between this ratio r and the Hauptmodul H, eliminating W_- between $P_-(W_-, H) = 0$ and $P_+(r \cdot W_-, H) = 0$, by performing a resultant. This resultant calculation yields a polynomial condition $P(r, H) = 0$, where the polynomial, of degree 36 in r and degree 18 in H, is the sum of 577 monomials. When $H = 0$ this polynomial reduces to

$$P(r, 0) = 2^{108} \cdot r^3 \cdot (4096\,r + 19683)^6 \cdot (4096\,r - 1)^{12} \cdot (r - 1)^6, \tag{C.9}$$

and when $H = 1$, it reduces to

$$\begin{aligned}
P(r, 1) = {} & (330225942528\,r^3 + 216854102016\,r^2 + 72695294208\,r + 1)^3 \\
& \times (16777216\,r^3 - 297467904\,r^2 + 2692418304\,r - 1)^6 \cdot (256\,r + 27)^9. \tag{C.10}
\end{aligned}$$

The equimodularity condition $|\kappa_+| = |\kappa_-|$ corresponds to an algebraic curve in the (x, y) complex plane ($z = x + i\,y$). This curve can be obtained by writing the Hauptmodul as a function of x and y, namely $H = X(x, y) + i\,Y(x, y)$, where $X(x, y)$ and $Y(x, y)$ are quite large rational expressions of x and y, and then parametrising the equimodularity condition $|r| = 1$ as $r = (1 - t^2)/(1 + t^2) + 2\,i\,t/(1 + t^2)$, where t is a real variable. This amounts to writing

$$P\left(\frac{1 - t^2}{1 + t^2} + i \cdot \frac{2\,t}{1 + t^2},\, X(x, y) + i\,Y(x, y)\right) = \mathcal{P}(x, y, t) + i \cdot \mathcal{Q}(x, y, t) = 0.$$

where $\mathcal{P}(x, y, t)$ and $\mathcal{Q}(x, y, t)$ are quite large rational expressions of the real variables x, y and t. Let us denote $\mathcal{N}_1(x, y, t)$ the numerator of $\mathcal{P}(x, y, t)$ and $\mathcal{N}_2(x, y, t)$ the numerator of $\mathcal{Q}(x, y, t)$. Eliminating t between $\mathcal{N}_1(x, y, t) = 0$ and $\mathcal{N}_2(x, y, t) = 0$, performing a resultant, one will get finally a quite large polynomial condition $\mathcal{P}(x, y) = 0$, corresponding to the algebraic equation of the equimodularity condition $|\kappa_+| = |\kappa_-|$.

Appendix C.2.1. Icosahedral symmetry of the equimodular curve

The polynomial condition is too large to be given explicitly here. It is, however, worth noting that, since the equimodular curve is deduced from polynomial expressions that depend only on the Hauptmodul H, the equimodular curve has the quite non-trivial property that it is compatible with the icosahedral symmetry of the hard hexagon model [30]. This icosahedral symmetry corresponds to the following

symmetry of the Hauptmodul (C.1). Let us introduce the complex variable ζ defined by $z = \zeta^5$, the fifth root of unity ω and the golden number τ

$$\omega = 1/4\sqrt{5} - 1/4 + 1/4\,i\sqrt{2}\sqrt{5 + \sqrt{5}}, \qquad \tau = \frac{1 + \sqrt{5}}{2}. \qquad (C.11)$$

Let us consider the order-five transformation h_5

$$\zeta \quad \longrightarrow \quad h_5(\zeta) = \tau \cdot \frac{\omega + (1 - \tau)\,\zeta}{\omega + \tau\,\zeta}. \qquad (C.12)$$

It is a non-trivial but straightforward calculation to see that the Hauptmodul H, seen as a function of the complex variable ζ, is actually invariant by this order-five transformation h_5, by the involution $\zeta \rightarrow -1/\zeta$ as well as the order-five transformation $\zeta \rightarrow \omega \cdot \zeta$:

$$H(\zeta) = H(h_5(\zeta)) = H\!\left(\frac{-1}{\zeta}\right) = H(\omega \cdot \zeta). \qquad (C.13)$$

Appendix C.2.2. A selected point of the equimodular curve

The algebraic equimodular curve $\mathcal{P}(x, y) = 0$ intersects the real axis $y = 0$ at the critical value z_c (i.e. $H = 0$, see (C.9)) and at an algebraic value $z = -5.94254104\cdots$ corresponding to the algebraic value of the Hauptmodul $H = 1.2699347\cdots$, a root of the polynomial $P_{12}(H)$ of degree twelve in H:

$$
\begin{aligned}
P_{12}(H) = {}& 4206595200930643574789609575 41^2 \cdot H^{12} \\
& - 30356761634507166731837844334358737657279358 68148497169025 \cdot 2^9 \cdot H^{11} \\
& + 180032218185835528405034756761309783218694171 171683152985 \cdot 2^{16} \cdot H^{10} \\[4pt]
& - 9639175985684877897319618325476027046477786920 96330233 \cdot 2^{25} \cdot H^9 \\
& + 468791798507154979087255598850059131881109892 4601809 \cdot 2^{33} \cdot H^8 \\
& - 117945240873473239544342529086996832814680875 05905 \cdot 2^{41} \cdot H^7 \\[4pt]
& + 3411125066039060170593037275840097714941325 0857 \cdot 2^{48} \cdot H^6 \\
& - 165628297151972865928725313935974053519244 79 \cdot 2^{57} \cdot H^5 \\[4pt]
& + 1043278670523689349628579379129299614704 1 \cdot 2^{65} \cdot H^4 \\
& - 445298098793697193619660365328834893 5 \cdot 2^{73} \cdot H^3 \\
& + 21846091895252252898479512333283 77 \cdot 2^{80} \cdot H^2 \\[4pt]
& - 14687865423363371951559480967168 \cdot 176160768^3 \cdot H \\
& + 956497920^6. \qquad (C.14)
\end{aligned}
$$

This algebraic point corresponds to the following algebraic values of $W_\pm$, in (C.4) and (C.3), $W_+ = -5404.2605\cdots$ and $W_- = 2118.9287\cdots + 971.5363\cdots i$, the ratio $r = W_+/W_-$ being, as it should, a complex number of unit modulus, namely $-0.3920\cdots + i\,.9199\cdots$ This algebraic point is characterized by the fact that W_+ or κ_+^6 (but not κ_-) is a real number: $\kappa_+^6 = 26.6786\cdots$ but $\kappa_- = 0.864\cdots - 1.497\cdots i$.

Appendix D. Cardioid fitting of partition function zeros

Examples of the excellent fit by the cardioid curve (43) of the inner boundary of the partition function zero on cylindrical lattices referred to in section 5.1.3 for the cases 33×33, 36×36 and 39×39 are plotted in figure D1. In figure D2 we plot the values of $a(L)$ and $c(L)$ the best fitted cardioid of (43) versus $1/L$ and observe that they are remarkable well fitted by a straight line which extrapolates as $L \to \infty$ to

$$a = 7.6302 \cdots \qquad c = -4.1268 \cdots \qquad (D.1)$$
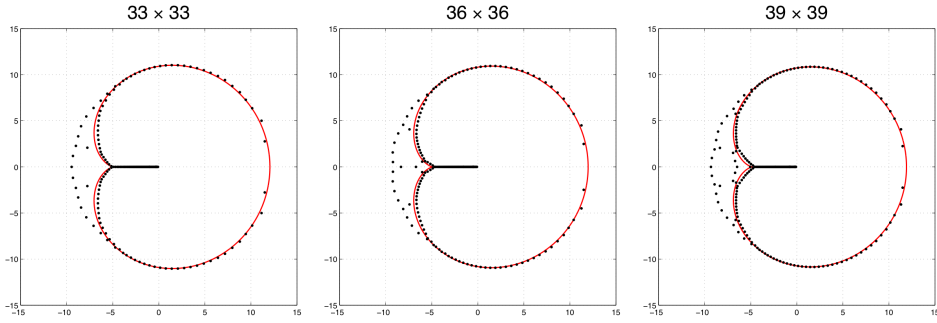
Figure D1. Fitting of the partition function zeros for cylindrical boundary conditions to the cardioid of (43) for the 33×33, 36×36 and 39×39 lattice.
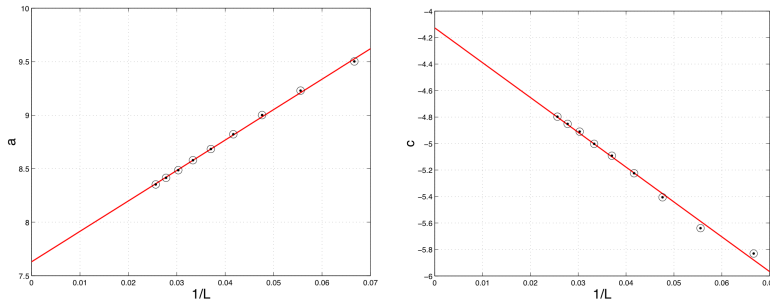
Figure D2. The fitting parameters a and c for cylindrical boundary conditions of the cardioid (43) versus L for the partition zeros of the $L \times L$ lattice.

Appendix E. Transfer-matrix algorithms
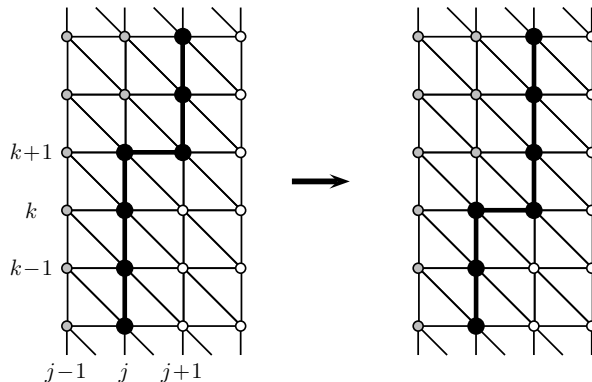
Figure E1. The movement of the transfer-matrix cut-line in the general case.

To calculate the partition functions $Z_{L_v,L_h}(z)$ we use what are known as 'transfer matrix' techniques. These work by moving a cut-line through the lattice and constructing a partial partition function for each possible configuration/state of sites on the cut-line. The most efficient way of calculating the partition function is to build up the lattice site-by-site as illustrated in figure E1. Sites on the cut-line are shown as large solid circles. Each of these sites can be either empty or occupied. Because of the hard particle constraint, nearest neighbors cannot be occupied simultaneously. So any configuration can be mapped to a binary integer in an obvious fashion with empty sites mapped to 0 and occupied sites to 1. The distinct configurations along the cut-line are thus circular n-bit strings with no repeated 1's. Their number is given by the Lucas numbers $L(n)$ (sequence A000204 in the OEIS [31]), which have the simple recurrence $L(n) = L(n-1) + L(n-2)$. In fact, $L(n) = (1+\sqrt{5})/2)^n + (1-\sqrt{5})/2)^n$, so the number of allowed configurations has the growth constant $(1 + \sqrt{5})/2 = 1.618\ldots$, and are therefore exponentially rare among the integers. Hence as is standard in such a case we use hash tables as our basic data structure to store and access the sparse array representing the state space of the model.

For each configuration we maintain a partial partition function (sum over all states) for the lattice sites already visited with each occupied site given weight z and each empty site given weight 1. The shaded circles in figure E1 represent sites already fully accounted for, that is, all possible occupancies have been summed over. The open circles are sites that are yet to be visited and hence are not yet accounted for. The black circles are not yet fully accounted for since their possible 'interactions' with the open sites have not yet been included. The movement of the cut-line in figure E1 consists of a move from the site at position $(j, k+1)$ to the 'new' site at position $(j+1, k)$ with 'interactions' with the neighbor sites at (j, k) and $(j + 1, k + 1)$. Notice that the update of the partial partition functions does not depend on the state of any other sites on the cut-line. Formally we can view the update as a matrix multiplication $\mathbf{w} = \mathbf{T}\mathbf{v}$, mapping the vector of partition functions $\mathbf{v}$ prior to the move to the vector of partition functions $\mathbf{w}$ after the move. The great advantage of the site-by-site updating is that we need not store the actual transfer matrix $\mathbf{T}$; it is given implicitly by a set of simple updating rules depending only on the 'local' configuration (states) of the sites

on the cut-line which are nearest neighbors to the new site.

We shall refer to the configuration of sites prior to the move as a 'source' and denote its integer representation with an S while a configuration after the move is referred to as a 'target' and denoted with a T. In an update we simply have to determine the allowed configuration of the 'new' site, that is, whether the new site is occupied or empty. The 'hard' constraint makes this very simple since the new site can be occupied only when all neighbor sites in the source configuration are empty. Since each site can be either empty (0) or occupied or (1) the four sites around the face have 16 possible configurations but only 6 are allowed because of the hard constraint. The 3 sites along the left and top form the 'local' source configuration and there are 5 (out of 8) allowed configurations. The local target configuration is given by the states of the 3 sites along the bottom and right of the face (2 sites occur in both source and target). By writing down the 6 allowed local configurations one can easily deduce the following simple updating rules

$$
\begin{aligned}
Z(T_{000}) &= Z(S_{000}) + Z(S_{010}), \\
Z(T_{100}) &= Z(S_{100}), \\
Z(T_{010}) &= z \cdot Z(S_{000}), \\
Z(T_{001}) &= Z(S_{001}), \\
Z(T_{101}) &= Z(S_{101}),
\end{aligned}
\tag{E.1}
$$

where the subscript triplets represent the states of the 'local' source sites at positions (j, k), $(j, k+1)$, $(j+1, k+1)$ and target sites at positions (j, k), $(j+1, k)$, $(j+1, k+1)$, respectively.

The transfer matrix algorithm described above takes care of the summation over sites in the interior of the lattice. Special rules apply at the top and bottom of a column. When adding a site at the top of a new column we include interactions between the site left of the new site and the site in the previous column on the bottom row (this interaction along a diagonal edge implements part of the periodic boundary condition in the L_h direction). Finally after we have completed a new column the site 'left over' in the previous column is superfluous to requirements and we can 'contract' the state space by summing over the states of this site. The number of distinct configurations for a column of height L_h sites is then $L(L_h + 1)$ for a partially completed column, and $L(L_h)$ when the column has been completed.

The transfer matrix algorithm described above is the same whether used in the calculation of partition function zeroes or eigenvalue crossings. Below we briefly outline how it is used in the two cases.

Appendix E.1. *Partition function zeros*

To calculate partition function zeros we need the exact partition function on an $L_v \times L_h$ lattice. This is simply a polynomial in z of degree $L_v \cdot L_h / 3$ with integer coefficients. So for each state along the cut-line the partial partition function is maintained as an array of integers of size $L_v \cdot L_h / 3 + 1$. The coefficients become very large and in order to deal with this the calculations were performed using modular arithmetic. So the calculation for a given size lattice was performed several times modulo different prime numbers with the full integer coefficients reconstructed from the calculated remainders using the Chinese remainder theorem. Utilizing the standard 32-bit integers we used

primes of the form $p_i = 2^{30} - d_i$, that is we used the set of largest primes smaller than 2^{30}. Depending on the L_v and L_h the number of primes required to reconstruct the exact integer coefficients can exceed 100. The zeros of the partition function can then be calculated numerically (to any desired accuracy) using root finders such as `MPSolve` [32] or `Eigensolve` [33]. We used `MPSolve` with a few calculations checked by using `Eigensolve`.

The transfer-matrix algorithm can readily be parallelised. One of the main ways of achieving a good parallel algorithm using data decomposition is to identify an invariant under the operation of the updating rules. That is, we seek to find some property of the configurations along the cut-line which does not alter in a single iteration. As mentioned above only the 'new' site can change occupation status. Thus, any site not directly involved in the update cannot change from being empty to being occupied and vice versa. This invariant allows us to parallelise the algorithm in such a way that we can do the calculation completely independently on each processor with just two redistributions of the data set each time an extra column is added to the lattice. This method for achieving a parallel algorithm has been used extensively for other combinatorial problems and the interested reader can look at [34] or [35, Ch 7] for details.

Cylindrical boundary conditions are simply implemented by starting the transfer matrix calculation with the all empty state having weight one (all other states having weight zero), iterating the algorithm to add L_h columns and then summing over all states.

Toroidal boundary conditions are fairly easy to implement but they are computationally expensive. The problem is that in order to include the interactions between sites in the first and last columns we have to 'remember' the state of the first column. Here we did this by simply specifying the initial state of the first column S_I, starting with the initial weights $Z(S) = 0$ when $S \neq S_\mathrm{I}$ and $Z(S_\mathrm{I}) = z^m$, where m is number of occupied sites in S_I. For each value of S_I we then perform the transfer matrix calculation as described above until the final column has been completed. Finally we put in the interactions between the occupation numbers in the last column with state S and those in the first column, sum over all states S, and repeat for all S_I. The saving grace is that one does not have to do this calculation for all values of S_I. Indeed, any S_I related by translational and reflection symmetry give rise to the same result. In table E1 we have listed the number of distinct initial states N_I one needs to consider in a calculation of the partition function with toroidal boundary conditions on a lattice of width L_h. The numbers N_I are given by sequence A129526 in the OEIS [31]. Note that for large L_h states which are invariant under the generators of the dihedral group D_{L_h} are exponentially rare. Therefore $L(L_h)/N_I \sim 2L_h$ for $L_h \gg 1$, and this is nicely brought out by the entries in table E1. Naturally the calculations for different initial states can be done completely independently making it trivial to parallelise over S_I (one can also fairly easily combine this with the parallel algorithm over state space should this be required).

The bulk of the large scale calculations for this part of the project were performed on the cluster of the NCI National Facility at ANU. The NCI peak facility is a Sun Constellation Cluster with 1492 nodes in Sun X6275 blades, each containing two quad-core 2.93GHz Intel Nehalem CPUs with most nodes having 3GB of memory per core (24GB per node). The largest size calculation we performed was for cylindrical boundaries where we went up to 39×39. This required the use of 256 processors (cores to be precise) taking around 140 CPU hours per prime with the calculation

L_h	N_I	$L(L_h)$	$L(L_h)/N_I$	L_h	N_I	$L(L_h)$	$L(L_h)/N_I$
3	2	4	2.00	6	5	18	3.60
9	9	76	8.44	12	26	18	12.38
15	64	1364	21.31	18	209	5778	27.64
21	657	24476	37.25	24	2359	103682	43.95
27	8442	439204	52.02	30	31836	1860498	58.44

Table E1. The number N_I of distinct initial states required to calculate the partition function with toroidal boundary conditions compared to the total number of states given by the Lucas numbers.

being repeated for 25 primes. The largest calculation for toroidal boundaries was the 27×27 lattice. This is sufficiently small memory wise to fit on a single core so we only used a parallelisation over initial states. The calculation took around 550 CPU hours per prime with the calculation repeated for 14 primes.

Appendix E.2. Transfer matrix eigenvalues

The equimodular curves on $L_h \times \infty$ strips where eigenvalues of largest modulus cross can be obtained from numerical studies using the transfer matrix algorithm outlined above. As we have seen, the dimension $\dim \mathbf{T}$ of the transfer matrix $\mathbf{T}$ for hard hexagons confined to a strip of height L_h grows exponentially fast with L_h. Hence the calculation of the eigenvalues of $\mathbf{T}$ and the resulting equimodular curves quickly becomes a very demanding task. We have however seen that the updating rules (E.1) do not require us to manipulate or store all the $(\dim \mathbf{T})^2$ entries of $\mathbf{T}$, but rather operate on two vectors of size $\dim \mathbf{T}$, namely $\mathbf{v}$ and $\mathbf{Tv}$, representing the set of conditional probabilities before and after a move of the cut-line. In other words, the trick of adding the sites to the system one at a time has produced a sparse-matrix factorization of $\mathbf{T}$.

It is possible to take further advantage of this gain to extract also the leading eigenvalues of $\mathbf{T}$. Namely, we use a set of iterative diagonalisation methods in which the object being manipulated is not $\mathbf{T}$ itself but rather its repeated action on a suitable set of vectors. An iterative scheme that works well even in the presence of complex and degenerate eigenvalues is known as Arnoldi's method [36]. This forms part of a class of algorithms called Krylov subspace projection methods [37]. These methods take full advantage of the intricate structure of the sequence of vectors $\mathbf{T^n v}$ naturally produced by the power method. If one hopes to obtain additional information through various linear combinations of the power sequence, it is natural to formally consider the Krylov subspace

$$\mathcal{K}_n(\mathbf{T}, \mathbf{v}) = \text{Span}\{\mathbf{v}, \mathbf{Tv}, \mathbf{T^2 v}, ..., \mathbf{T^{n-1} v}\}$$

and to attempt to formulate the best possible approximations to eigenvectors from this subspace. We make use of the public domain software package ARPACK [38] implementing Arnoldi's method with suitable subtle stopping criteria. The ARPACK package allows one to extract eigenvalues (and eigenvectors) based on various criteria, including the one relevant to our calculations, namely the eigenvalues of largest modulus.

The problem specific input for this type of calculation only consists in a user supplied subroutine providing the action of $\mathbf{T}$ on an arbitrary complex vector $\mathbf{v}$. In

our case this amounts to iterating the update rules (E.1) until a complete column has been added to the lattice. In particular, the sparse-matrix factorization and the subtleties having to do with the 'inflation' of the state space before the addition of the first site in a new row, as well as the 'contraction' after the addition of the last site in a completed row, are all hidden inside this subroutine and not visible to Arnoldi's method. The iterations of $\mathbf{T}$ are thus computed for a fixed complex value of the fugacity z until the ARPACK routines have converged.

Very briefly, we trace the equimodular curve as follows. First we find a point on the equimodular curve; we can choose a point on the negative real axis, say $z_0 = -1$, that we know is on the curve. To find a new point z on the curve we start at the previous point and look for a new point on a circle of radius ϵ (in general we use $\epsilon = 10^{-2}$) at an angle θ_0 from the previous point. In general this trial point will not lie on the equimodular curve. Our algorithm then finds a new point by using the Newton-Raphson method to converge in the angle θ towards a zero in the distance between leading eigenvalues. The pair (z, θ) is then used as the starting values (z_0, θ_0) for a new iteration of the search algorithm. This procedure in then iterated until the equimodular curve has been traced. Points where the curve branches are detected by noting that the third leading eigenvalue becomes equal in modulus to the leading eigenvalue. End points are detected by noting that the procedure cannot find a new point (in fact it turns around and converges towards a point on the part of the curve already traced). Many aspects of this search algorithm involve subtleties, in particular automatizing the procedure in the case where the equimodular curve has a complicated topology with many branchings; this will be described fully in a separate publication [39].

As for the partition function zeroes, we are interested in tracing the equimodular curves for both toroidal and cylindrical boundary conditions. Since in both cases we use the same transfer matrix $\mathbf{T}$ (i.e., with periodic boundary conditions in the L_h direction) it might seem that the curves would be identical. This is not the case. Indeed, in the cylindrical case the initial condition imposed on the first column of the lattice is that all sites in the preceding column are empty. In particular, this initial state is translational invariant and thus has momentum $P = 0$. This momentum constraint can be imposed by rewriting $\mathbf{T}$ in the translational and reflection symmetric subspace of dimension N_I. Once again, an appropriate 'inflation' and 'contraction' of the state space has to be performed at the beginning and the end of the user supplied subroutine, as the kink on the cut-line describing the intermediate states breaks the dihedral symmetries explicitly. But since these intermediate steps are hidden from Arnoldi's method, the end result amounts to diagonalising a transfer matrix of smaller dimension, $\dim \mathbf{T} = N_I$. Meanwhile, the equimodular curve for toroidal boundary conditions is obtained by diagonalising the original transfer matrix without the $P = 0$ constraint, i.e., with dimension $\dim \mathbf{T} = L(L_h)$.

The memory requirements of the algorithm up to the largest size $L_h = 30$ that we attempted is quite modest and the calculation can be performed on a basic desktop or laptop computer. As an example the calculation of the equimodular curve for $L_h = 30$ with cylindrical boundary conditions took about 10 days on a MacBook Pro with a quad core I7 2.3GHZ processor.

Appendix F. Finite-size scaling analysis of $z_c(L)$ and $z_d(L)$

According to the theory of finite-size scaling (FSS) [40], the free energy per site corresponding to the j-th eigenvalue of the transfer matrix has the scaling form

$$\frac{1}{L} f_j \left(|z - z_c| L^y, u L^{-|y'|} \right) , \tag{F.1}$$

where z_c is the critical point, y is the leading relevant eigenvalue under the renormalization group (RG), and u is the coupling to an RG irrelevant operator with eigenvalue $y' < 0$. If more than one RG irrelevant coupling is present there will be further arguments to the function, which we here omit for clarity. The equimodularity condition $|f_1| = |f_2|$ can obviously be written in the same scaling form as can the partition function zeros. Moreover, FSS assumes that the functions f_j are analytic in their arguments for $z \neq z_c$, which implies at leading order that

$$|z - z_c| = A L^{-y} + B u L^{-y - |y'|} + \dots , \tag{F.2}$$

where A and B are non-universal constants. To higher orders, the terms appearing on the right-hand side involve powers of L^{-1} that can be any non-zero linear combination of y and $|y'|$ with non-negative integer coefficients. There is obviously no guarantee that all such terms will appear, since some of the multiplying constants $(A, B, \dots)$ may be zero.

When it is known that $z \to z_c$ as $L \to \infty$, with z_c real, one can similarly analyze distances other than $|z - z_c|$ to the critical point that vanish linearly with $z - z_c$. Examples include $||z| - z_c|$, $\mathrm{Re}(z) - z_c$, $\mathrm{Im}(z)$, and $\mathrm{Arg}(z)$.‡ According to the general principles of FSS [40] these variables can be developed on $|z - z_c|$ and the irrelevant RG couplings, and (F.2) will follow, albeit necessarily with different values of the non-universal constants $(A, B, \dots)$.

The critical point $z_c > 0$ in the hard hexagon model is known to be in the same universality class as the three-state ferromagnetic Potts model [41]. The energy operator of the latter [42] provides the RG eigenvalue $y = 2 - 2h_{2,1} = 6/5$, where we have used the Kac table notation $h_{r,s}$, familiar from conformal field theory (CFT), for the conformal weight of a primary operator $\phi_{(r,s)}$. Subdominant energy operators, $\phi_{(3,1)}$ and $\phi_{(4,1)}$, follow from CFT fusion rules and lead to RG eigenvalues $y' = -4/5$ and $y'' = -4$ respectively. Our numerical analysis of $|z_c(L)| - z_c$ for L up to 39 (see table 5) gives good evidence for the FSS form

$$|z_c(L)| - z_c = a_0 L^{-6/5} + a_1 L^{-2} + a_2 L^{-14/5} + \dots . \tag{F.3}$$

The powers of L^{-1} appearing on the right-hand side can be identified with y, $y + |y'|$ and $y + 2|y'|$. This is compatible with the above general result; note however that the power $2y = 12/5$, which is a priori possible, is not observed numerically.

The CFT of the Lee-Yang point $z_d < 0$ is much simpler [16], since there is only one non-trivial primary operator $\phi_{(2,1)}$. It provides the RG eigenvalue $y = 12/5$. Our numerical analysis of $|z_d(L) - z_d|$ (see table 5) gives strong evidence for the FSS form

$$|z_d(L) - z_d| = b_0 L^{-12/5} + b_1 L^{-17/5} + b_2 L^{-22/5} + \dots . \tag{F.4}$$

The powers of L^{-1} on the right-hand side can be identified with y, $y + 1$ and $y + 2$. The integer shifts in (F.4) can be related to descendent operators in the CFT, since

‡ Obviously we here exclude cases where the variable is identically zero, such as when $\mathrm{Im}(z) = 0$, or when $||z| - z_c| = 0$ because of a circle theorem.

$|y'|$ is a positive integer for descendents of the identity operator; note that some descendents are ruled out by symmetry arguments, as in section 5.3. Another source of corrections in powers of L^{-1} is that the data of table 5 are computed for $L \times L$ systems with cylindrical boundary conditions. Indeed, while the length L along the periodic direction is unambiguous, the one along the free direction should possibly be interpreted as $L + a$ in the continuum limit, where a is a constant of order unity. In any case, it is remarkable that $y + 1 = 11/5$ does not occur in (F.4).

To probe the finite-size scaling form, i.e., determine which terms actually occur in the asymptotic expansion, we carry out a careful numerical analysis of how the endpoints $z_d(L)$ and $z_c(L)$ approach z_d and z_c in the thermodynamic limit. Since our data for end-point positions is most extensive in the case of partition function zeros with cylindrical boundary conditions we analyse the data of table 5. We also tried to analyse the data in table 3 obtained from equimodular calculations, but we found that this data set suffers from numerical instability presumably because our determination of the end-point position is not sufficiently accurate. Note that the data in table 5 can be calculated to any desired numerical accuracy since it is obtained from the zeros of polynomials. Obviously the data for $z_d(L)$ is much closer to the thermodynamic limit z_d than is the corresponding data for $z_c(L)$ so it is no surprise that the analysis of $z_d(L)$ is 'cleaner' than that for $z_c(L)$ and hence we start our exposition with the former.

Firstly, plotting $\ln|z_d(L) - z_d|$ versus $\ln L$ confirms a power-law relationship (see left panel of figure F1). To estimate the exponent we take a pair of points at L and $L - 3$, calculate the resulting slope of a straight line through the data-points, and in figure F1 we plot the slope versus $1/L$. Clearly, the slope can be extrapolated to the predicted value, $12/5$, for the exponent. We next look for sub-dominant exponents. Accepting the $12/5$ exponent as exact we form the scaled sequence, $s(L) = L^{12/5}|z_d(L) - z_d| \simeq a + b/L^\alpha$, and look at the sequence of differences, $d(L) = s(L) - s(L - 3) \propto 1/L^{\alpha+1}$, thus eliminating the constant term. As before we calculate the slope of $\ln d(L)$ versus $\ln L$ and plot against $1/L$. From figure F1 the slope is seem to extrapolate to a value of -2, so $\alpha = 1$ and hence the sub-dominant exponent is $17/5$. We then repeat the analysis starting with the $d(L)$ sequence which we scale by L^2. The estimates for the local slopes are shown in figure F1 and are again consistent with a slope of -2, indicating that the third exponent in the asymptotic expansion is $22/5$.

From the above analysis we conclude that the correct asymptotic form is (F.4). It is tempting to conjecture that the sequence of integer spaced corrections $L^{-12/5-k}$ will continue indefinitely. However, we cannot completely rule out the presence of extra terms such as $L^{-n\cdot 12/5}$ for $n \geq 2$. This is borne out by a further analysis using five terms in the asymptotic expansion namely the three exponents firmly established above and a further two terms with exponents $2y = 24/5$, $y + 3 = 27/5$, and $y + 3 = 27/5$, $y + 4 = 32/5$, respectively. The resulting amplitude estimates are shown in figure F2. Clearly, the fits using only terms of the form $y+k$ display much less variation against $1/L$ and this could be an indication that only these types of terms are present in the asymptotic expansion. However, the amplitude b_3 when fitting using an exponent $24/5$ does not appear to vanish and hence we are not willing to claim with certainty that this term is absent. If we assume only terms of the form $y + k$, we can obtain refined amplitude estimates by truncating the expansion after a fixed number of terms and fitting using sub-sequences of consecutive data points. Results
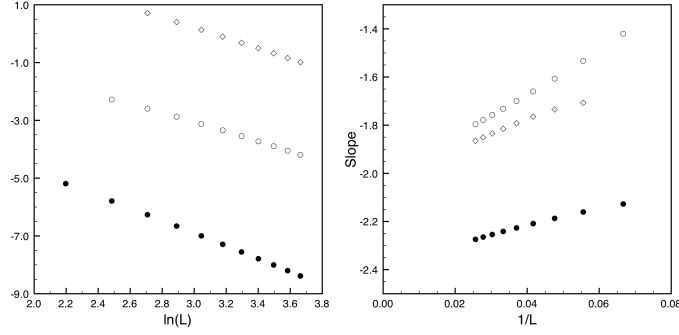
Figure F1. The left panel are log-log plots of the data for $|z_d(L) - z_d|$ (filled circles), $d(L)$ (open circles) and $L^2 d(L) - (L-3)^2 d(L-3)$ (diamonds). In the right panel we plot the corresponding local slopes versus $1/L$.

for the leading amplitude b_0 are displayed in figure F3. Note that the estimates are quite accurate and that as more terms from the asymptotic expansion are included the estimates have less variation. We estimate that

$$b_0 = 1.7147(1), \quad b_1 = -9.30(2), \quad b_2 = 48(2), \quad b_3 = -180(30). \text{ (F.5)}$$
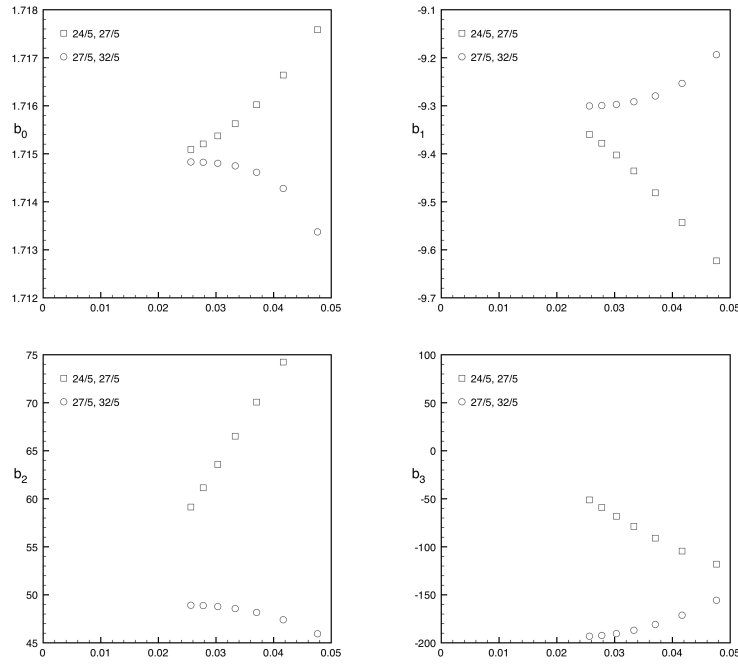
Figure F2. Amplitude estimates versus $1/L$ when fitting to a five-term asymptotic form akin to (F.4), but with two additional exponents as indicated on the plots.

We now turn to $z_c(L)$ where we start by analysing the data for $|z_c(L)| - z_c$. Note that the modulus $|z_c(L)|$ can be viewed as a crude approximation to where the zeros
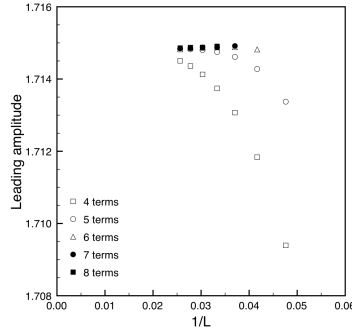
Figure F3. Estimates for the leading amplitude b_0, plotted versus $1/L$ in the asymptotic expansion (F.4) when truncating after 4 to 8 terms and using only exponents $24/5 + k$.

intercept the real axis since it amounts to saying that the zeros approach the real axis along a circle. Many other measures of the distance/approach to z_c could be used but this one happens to be particularly well-behaved so we start our exposition with this quantity. As above we first look at the local log-log slope for this data shown in the left panel of figure F4. In this case the data displays pronounced curvature but nevertheless it seems reasonable that the slope can be extrapolated to the predicted value $-6/5$. We next look for sub-dominant exponents. Accepting the $6/5$ exponent as exact we form the scaled sequence, $s(L) = L^{6/5}(|z_c(L)| - z_c) \simeq a + b/L^\alpha$. We again look at the sequence $d(L)$ of differences and plot the local slopes in the right panel of figure F4 using open circles. In this case the results are not as clear cut. The data can be extrapolated to a value > -2 and it is consistent with the predicted exponent $y + |y'| = 2$, which would yield a slope of -1.8. We then repeated the analysis scaling $d(L)$ by $L^{9/5}$ and looking at the differences. The local slopes are shown as diamonds in the right panel of figure F4. Clearly no meaningful extrapolation can be performed on this data other than to say that a value of -1.8 cannot be ruled out.
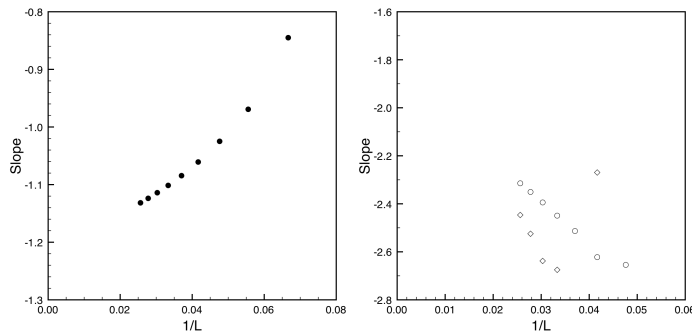
Figure F4. Local slopes versus $1/L$ for $||z_c(L)| - z_c|$ in the left panel and in the right panel the sequences $d(L)$ (open circles) and $L^{9/5}d(L) - (L-3)^{9/5}d(L-3)$ (diamonds).

To further investigate the asymptotic scaling form we turn to amplitude fitting using

$$|z_c(L)| - z_c = a_0/L^{6/5} + a_1/L^{10/5} + a_2/L^\Delta. \qquad \text{(F.6)}$$

We look at three possible values for the third exponent Δ, namely $y + 1 = 11/5$, $2y = 12/5$, or $y + 2|y'| = 14/5$. The results are displayed in figure F5 where we plot the estimated values of the three amplitudes for the three different values of Δ. Firstly, we note that the estimates for the amplitude a_0 (left panel) are quite stable though the estimates become more stable as the value of Δ is increased. Secondly, the data for the amplitude a_1 (middle panel) is very striking; for a Δ of $11/5$ or $12/5$ the estimates vary greatly with L and even have the wrong sign from the extrapolated value; in sharp contrast for $\Delta = 14/5$ the estimates are quite well converged with only a mild dependence on L. Finally, for the amplitude a_2 (right panel) we see that the amplitude estimates for $\Delta = 11/5$ or $12/5$ may well extrapolate to a value of 0 while the estimates for $\Delta = 14/5$ clearly extrapolate to a non-zero values around -200 or so. Taken together this is quite clear evidence that the correct value of the third exponent is $\Delta = y + 2|y'| = 14/5$. We estimate roughly that

$$a_0 = 53.0(1), \quad a_1 = -50(5), \quad a_2 = -200(50). \qquad \text{(F.7)}$$
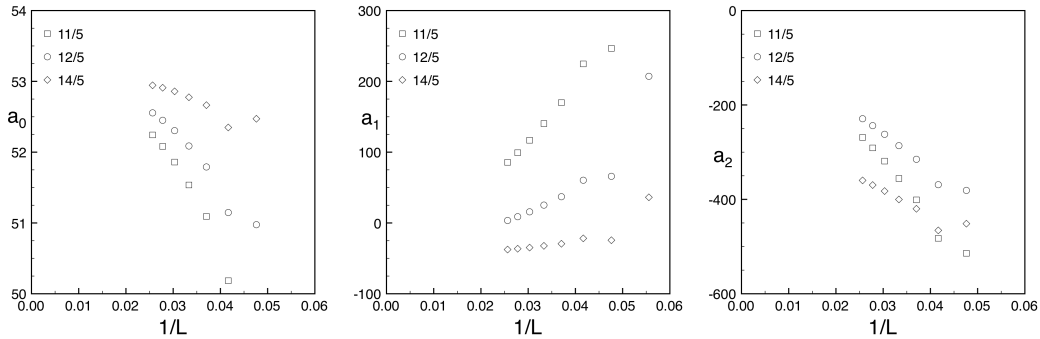
Figure F5. Amplitude estimates versus $1/L$. The panels (from left to right) shows the estimates for the amplitudes a_0, a_1 and a_2 when fitting to the asymptotic form (F.6) while using three different values for the third exponent Δ.

In figure F6 we plot the data for $|z_c(L)| - z_c$ (left panel) and $|z_d(L) - z_d|$ (right panel) and the asymptotic fits obtained above.

It is universally expected that the end-point $z_c(L)$ converges towards z_c, as can be confirmed by analyzing the behavior of $\text{Re}(z_c(L))$ and $\text{Im}(z_c(L))$ against $1/L$. This obviously means that the imaginary part must vanish as $L \to \infty$. To examine this we repeat the above analysis for $\arg(z_c(L))$. The 'local-slope' analysis is not as clear-cut in this case but it is consistent with the two leading terms in (F.6). The amplitude analysis is again very clean as can be seen in figure F7 and from this we obtain the amplitude estimates

$$a_0 = 15.83(2), \quad a_1 = -3.0(5), \quad a_2 = 8(2). \qquad \text{(F.8)}$$

These values of course differ from those in (F.7) since we are analyzing a different quantity.

Finally we carried out a similar analysis for the quantity $|z_c(L) - z_c|$. Again the evidence for the leading amplitude being $-6/5$ was firm. However, the local-slope analysis for the sub-dominant term was inconclusive. In figure F8 we plot the
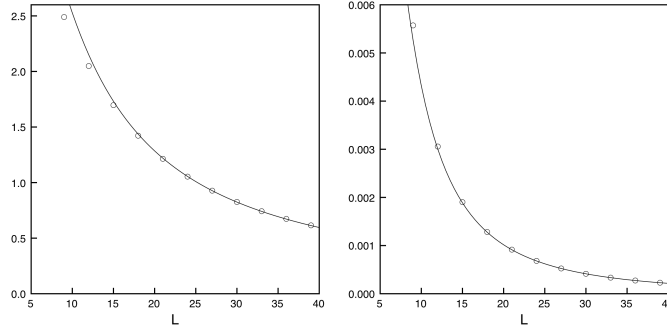
Figure F6. Data for $|z_c(L)| - z_c$ (left panel) and $|z_d(L) - z_d|$ (right panel) and fitted curves to the asymptotic forms (F.3) and (F.4) using the listed amplitude estimates (F.7) and (F.5).
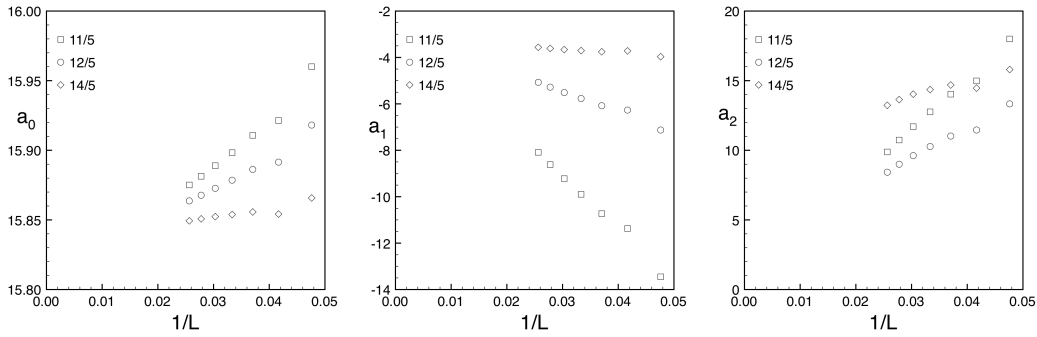
Figure F7. Amplitude estimates versus $1/L$. The panels (from left to right) shows the estimates for the amplitudes a_0, a_1 and a_2 when fitting $\arg(z_c(L))$ to the asymptotic form (F.6) while using three different values for the third exponent Δ.

amplitude estimates obtained when fitting to (F.3). We observe a very strong variation in a_1 and a_2, but on the other hand the amplitude estimates are nice and monotonic, suggesting that the data might just be really hard to fit. In particular we note that a_1 could extrapolate to 0. We then tried a new fit using an additional fourth term with exponent $-18/5$, thus assuming exponents of the form $y + k|y'| = 6/5 + k \cdot 4/5$ In this case we found much more stable amplitude estimates with $a_0 = 183.5(5)$. The other amplitudes displayed quite a bit of scatter so we will not quote error-bars, but we found $a_1 \simeq 6.5$, $a_2 \simeq 930$ and $a_3 \simeq -5200$. Remarkably a_1 is quite small compared to the other quantities which may well explain the numerical difficulties we had with the analysis. Note that we make no claim that $y + k|y'|$ exhausts the exponents and it is quite likely that other exponents, such as $2y + |y'| = 16/5$, could occur, but our data sets are too limited to answer such questions beyond the terms explicitly included in (F.3).
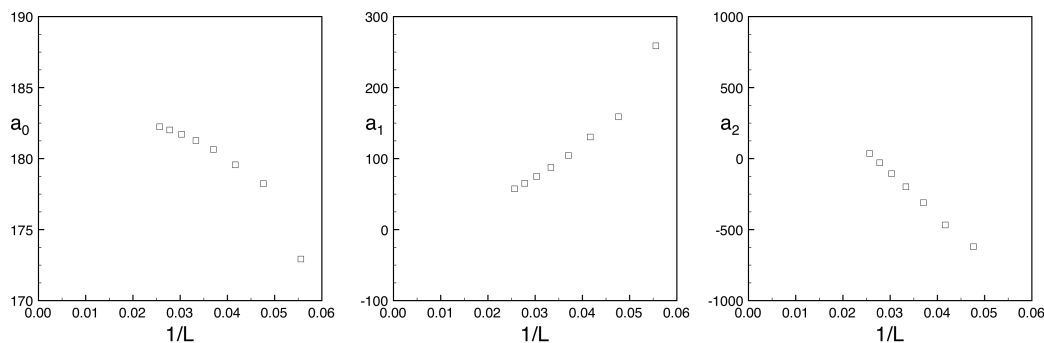
Figure F8. Amplitude estimates versus $1/L$. The panels (from left to right) shows the estimates for the amplitudes a_0, a_1 and a_2 when fitting to the asymptotic form (F.3) while using the data for $|z_c(L) - z_c|$.

References

[1] Baxter R.J 1980, Hard hexagons: Exact Solution, J. Phys. **A 13** L61-L70.
[2] Baxter R.J 1982, Exactly Solved Models in Statistical Mechanics, (Academic Press).
[3] Yang C.N and Lee T.D 1952, Statistical theory of equations of state and phase transitions. I. Theory of condensation model, Phys. Rev. **87** 406-409.
[4] Baxter R. J 1987, Chromatic polynomials of large triangular lattices, J. Phys. **A 20** 5241-5261.
[5] Joyce G.S 1988, On the hard-hexagon model and the theory of modular functions, Phil. Trans. R. Soc. Lond. **A 325** 643-702.
[6] Fendley D, Schoutens K and van Eerten H 2005, Hard squares with negative activity, J. Phys. **A 38** 315-322.
[7] Jonsson J 2006, Hard squares with negative activity and rhombus tilings of the plane, Electron. J. Combin. **13** (1) #R67.
[8] Bousquet-Mélou M, Linusson S, and Nero E 2008, On the independence complex of square grids, J. Algebraic Combin. **27** (4) 423-450.
[9] R.J. Baxter, Hard squares for $z = -1$, Ann. Comb. 15 (2011) 185-195.
[10] Beraha S, Kahane J and Weiss N.J 1975, Proc. Nat. Acad. Sci. USA **72** 4209.
[11] Beraha S and Kahane J 1979, J. Combin. Theory **B 27** 1.
[12] Beraha S, Kahane J and Weiss N.J 1980, J. Combin. Theory **B 28** 52.
[13] Salas J and Sokal A.D 2001, Transfer matrices and partition-function zeros for antiferromagnetic Potts models. I. General theory and square lattice chromatic polynomial, J. Stat. Phys. **104** 609-699.
[14] Baxter R. J and Pearce P.A 1982, Hard hexagons: interfacial tension and correlation length, J. Phys. **A 15** 897-910.
[15] C. Itzyksom, R.B. Pearson and J.B. Zuber 1983, Distribution of zeros in Ising and gauige models, Nucl. Phys. **B220[FS8]** 415-433.
[16] Cardy J.L 1985, Conformal invariance and the Yang-Lee edge singularity in two dimensions, Phys. Rev. Letts. **54** 1354-1356.
[17] Dotsenko, Vl. s. 1984, Critical behavior and assosciated conformal algebra of the z_3 Potts model, J. Stat. Phys. **34** 781-791.
[18] Dhar D 1983, Exact solution of a directed-site animals-enumeration problem in three dimensions, Phys. Rev. Letts. **51** 853-856.
[19] J. L. Jacobsen 2007, Exact enumeration of Hamiltonian circuits, walk and chains in two and three dimensions, J. Phys. A **40** 14667–14678.
[20] J.L. Cardy, private communication
[21] S-N Lai and M.E. Fisher 1995, The universal repulsive-core singularity and Yang-Lee edge criticality, J. Chem. Phys. 103, 8144-8155.
[22] Park Y and Fisher M.E 1999, Identity of the universal repulsive-core singularity with Yang-Lee edge criticality, Phys. Rev. **E 60** 6323-6328.
[23] Groeneveld J 1962, Two theorems for classical many particle systems, Phys. Letts, **3** 50-51.
[24] Wood D.W 1985, The exact location of partition function zeros, a new method for statistical

mechanics, J. Phys. A **18** L917-L921.

[25] Wood D.W 1987, The algebraic construction of partition function zeros: universality and algebraic cycles, J. Phys. A20 3471-3493.

[26] Wood D.W, Turnbull R.W and Ball J.K 1987, Algebraic approximations to the locus of partition function zeros; J. Phys. **A 20** 3495-3521.

[27] Wood D.W, Turnbull R.W and Ball J.K 1989, An observation on partition function zeros of the partition function of the hard hexagon model, J. Phys. **A 22** L105-L109.

[28] Richey M. P and Tracy C.A 1987, Equation of state and isothermal compressibility for the hard hexagon model in the disordered regime, J. Phys. **A 20** L1121-L1126.

[29] Tracy C.A, Grove L and Newman F.M 1987 Modular properties of the hard hexagon model, *J. Stat. Mech.* **48**, Issue 3-4, pp 477-502

[30] Joyce G.S 1989, On the icosahedral equation and the locus of zeros of the hard-hexagon model, J. Phys. **A 22** L237-L242.

[31] The On-Line Encyclopedia of Integer Sequences at `http://oeis.org`.

[32] Bini D and Fiorentino G 2000, Numer. Algorithms **23**, 127.

[33] Fortune S 2002, J. Symb. Comput. **33**, 627.

[34] Jensen I 2003 A parallel algorithm for the enumeration of self-avoiding polygons on the square lattice *J. Phys. A: Math. Gen.* **36** 5731–5745

[35] Guttmann A J, ed. 2009 *Polygons, Polyominoes and Polycubes* vol. 775 of *Lecture Notes in Physics* (Springer)

[36] Arnoldi W E 1951, The principle of minimized iterations in the solution of the matrix eigenvalue problem, Quart. Appl. Math. **9**, 17–29.

[37] Saad Y 1992, Numerical methods for large eigenvalue problems, Algorithms and architectures for advanced scientific computing, (Manchester University Press, Manchester).

[38] RB Lehoucq, DC Sorensen, and C Yang, *ARPACK Users' Guide*, Software, Environments, and Tools (SIAM, 1998).

[39] Jacobsen J L and Jensen I 2013 (in preparation).

[40] Cardy J L 1996, *Scaling and renormalisation in statistical physics*, Cambridge University Press.

[41] Wu F Y 1982, Rev. Mod. Phys. **54**, 235-268.

[42] Dotsenko Vl S 1984, Critical behavior and associated conformal algebra of the Z_3 Potts model, J. Stat. Phys. **34**, 781–791.